

Robust Real-Time Multi-View Eye Tracking

Nuri Murat Arar, *Student Member, IEEE*, and Jean-Philippe Thiran, *Senior Member, IEEE*

Abstract—Despite significant advances in improving the gaze estimation accuracy under controlled conditions, the tracking robustness under real-world conditions, such as large head pose and movements, use of eye glasses, illumination and eye type variations, remains a major challenge in eye tracking. In this paper, we revisit this challenge and introduce a real-time multi-camera eye tracking framework to improve the estimation robustness. First, differently from previous work, we design a multi-view tracking setup that allows for acquiring multiple eye appearances simultaneously. Leveraging multi-view appearances enables to more reliably detect gaze features under challenging conditions, particularly when they are obstructed due to large head movements and glasses effects in conventional single-view appearance. The features extracted on various appearances are then used for estimating multiple gaze outputs. Second, we propose to combine the gaze outputs through an adaptive fusion mechanism in order to compute user’s overall point of regard. The proposed mechanism firstly determines the estimation reliability of each gaze output according to user’s momentary head pose and general gazing behavior, and then performs a reliability-based weighted fusion. We demonstrate the efficacy of our framework with extensive simulations and user experiments on a collected dataset featuring 20 subjects. Our results show that in comparison with state-of-the-art eye trackers, the proposed framework provides not only a significant enhancement in accuracy but also a notable robustness. Our prototype system runs at 30 frames-per-second (fps) and achieves $\sim 1^\circ$ accuracy under challenging experimental scenarios, which makes it suitable for various high-precision demanding applications.

I. INTRODUCTION

Gaze movements provide cues indicating observer’s visual attention, emotional state and cognitive processes [1], [2]. Therefore, tracking eye and gaze movements, also known as eye tracking, is essential for human behaviour research applied in a wide variety of disciplines, including among many others, sociology, psychology, cognitive science, neuroscience, and marketing research. Besides, it is an important modality to enhance human-computer interaction for controlling and navigation. The popularity of eye tracking has recently been increasing, owing to the promising advancements made. Despite valuable efforts, high-accuracy ($\sim 1^\circ$) eye tracking systems still suffer from various factors, such as high setup complexity, inflexible system configurations, high cost, tedious user calibration procedures, and more importantly, low tolerance to varying real-world conditions, which hinder them from being widely used. Hence, there is still room for further research efforts, particularly towards improving their accuracy and robustness under unconstrained conditions.

Remote video-oculography, in which users’ eyes are non-intrusively captured by remote sensors, is the focus of this paper since it provides the most natural and convenient interaction for the users. As described in a recent survey [3], remote sensor-based eye tracking methods can be classified mainly

into two categories, namely, *appearance-based* and *feature-based*. *Appearance-based* methods use the image content as the input. They learn a mapping from the image features directly to the gaze points. On the other hand, *feature-based* methods utilize local features extracted on eye images, such as pupil center and reflections on the cornea (aka glints), to determine the gaze. They mostly require particular hardware configuration and leverage the features that are formally related to the gaze points through the geometry of the system and eye physiology. *Feature-based* methods can further be categorized into *3D model-based*, *regression-based*, and *cross ratio-based* methods. Each category has its own advantages and disadvantages in terms of the estimation accuracy, robustness, and system implementation complexity, as summarized in Table I. *3D model-based* methods [4]–[8] compute the gaze from the eye features obtained from a 3D geometric eye model, whereas *regression-based methods* [9]–[12] assume a direct mapping from the eye features to the gaze points. On the other hand, *cross ratio-based methods* [13]–[18] compute the gaze by leveraging the cross ratio property of the projective space.

Over more than two decades, numerous works from each of the aforementioned categories have been presented. Among these, the main emphasis has been mostly given to the estimation accuracy improvements through introducing different gaze models [6], [13] and systems [10], [19], or developing better person-specific bias correction techniques [17]–[21]. Consequently, very high estimation accuracies ($< 1^\circ$) are reported under controlled conditions. Nevertheless, the research and validation of the tracking robustness under real-world conditions, such as large head movements, use of eyewear, variations in illumination and eye type, have been largely neglected. Thus, these remain major concerns in eye tracking.

In this paper, extending our previous effort that focus on improving the estimation accuracy [19], we address the major robustness concerns of current eye tracking systems. We present a real-time multi-view gaze estimation methodology to improve the tracking robustness to real-world conditions. Instead of tracking the gaze from a single view as performed by previous work, we design a multi-view framework to leverage multiple eye appearances simultaneously acquired from various views. In conventional single-view setups, there exists a single appearance, on which the features may be obstructed due to challenging conditions such as large head movements and occlusions caused by glasses. Whereas in our framework, the main benefit is to simultaneously perform feature detection on multi-view appearances. For each frame, our approach enables to compute multiple gaze outputs using the extracted features. Furthermore, these gaze outputs are effectively combined by a novel adaptive fusion mechanism to compute user’s overall point of regard (PoR). In this context, the proposed mechanism firstly determines the estimation

N. M. Arar and J.-P. Thiran are with the Signal Processing Laboratory (LTS5), École Polytechnique Fédérale de Lausanne (EPFL), Switzerland.

TABLE I: A generic comparison of gaze estimation techniques.

Evaluation Criteria	3D Model-based	Regression-based	Cross Ratio-based	Appearance-based
Setup complexity:	high	medium	medium	low
System calibration:	fully-calibrated	×	×	×
Hardware requirements (# of cameras):	2+ infrared (stereo)	1+ infrared	1+ infrared	1+ ordinary
Hardware requirements (# of lights):	2+ infrared	2+ infrared	4+ infrared	×
Gaze estimation accuracy error:	$< 1^\circ$	$\sim 1 - 2^\circ$	$\sim 1 - 2^\circ$	$> 2^\circ$
Implicit robustness to head movements:	medium-high	low-medium	low-medium	low
Implicit robustness to varying illumination:	medium-high	medium-high	medium-high	low
Implicit robustness to use of eyewear:	low	low	low	medium

reliability of each gaze output according to the proposed gaze reliability indicators such as user's general gazing behavior and momentary head poses with respect to each camera. Then, it performs a reliability-based weighted fusion, which leads to improved accuracy and robustness. Extensive evaluations on both simulated and real-world data were performed to validate our methodology. In addition to thorough simulations, a database featuring 20 users performing eight experiments under varying illumination conditions and head movements was collected. In these experiments, natural human-computer interaction was targeted. Users followed some conventional experimental scenarios as well as a newly introduced one. The results demonstrate that in comparison to conventional single-view eye tracking, our multi-view approach provides a significantly better performance both in accuracy and robustness to aforementioned challenging conditions.

The proposed framework is highly flexible and can easily adapt to hardware and software modifications. Depending on the application type and desired tracking performance, the employed gaze estimation method, number of cameras and their configuration can simply be alternated, even without requiring any system adjustments (e.g., camera or geometric scene calibration) for uncalibrated settings. Our current uncalibrated prototype relies on a *cross ratio-based* gaze estimation method, and operates with low-resolution eye data. The system's overall hardware setup and computational complexities are lower than those of fully-calibrated systems. Hence, it enables a fast and accurate eye tracking without requiring any cumbersome camera and geometric scene calibrations. Our three-camera prototype system outputs PoRs with an accuracy of $\sim 1^\circ$ at 30 fps and also obtains nearly 100% estimation availability under challenging scenarios.

The outline of the paper is described as follows: Section II gives an overview of the related work. Section VIII describes the proposed framework. Evaluations on the simulated and real data are presented in Section IV and IX. Section VI discusses the acquired insights, and conclusions are given in Section VII.

II. RELATED WORK

A generic comparison of existing eye tracking solutions regarding various evaluation criteria is given in Table I. The following presents an overview of the related work.

A. Gaze Estimation Accuracy & Setup Complexity

The majority of the existing work focus on improving the estimation accuracy. There is no doubt that the accuracy is directly proportional to the setup complexity. *3D model-based* methods [4]–[7], [22] are widely preferred as they provide high accuracy under generic head movements, owing to their

explicit and fine 3D eye modeling. Most commercial eye tracking solutions rely on *3D model-based* methods. However, they have a significant drawback, that is to require fully-calibrated systems. To acquire an accurate 3D eye model, a complex setup that requires camera and geometric scene calibrations (e.g., stereo, depth sensor) is needed. Alternatively, *cross ratio-based* [13]–[19] and *regression-based* methods [12], [23] have mostly lower setup complexity and avoid setup calibrations. However, they are approximate solutions, and so, their performances are unfortunately lower in accuracy and movement robustness. On the contrary to *feature-based* methods, *appearance-based* methods [24]–[27] simply require an ordinary camera. Yet, they are restricted to particular applications due to their limitations in accuracy and robustness.

The great majority of the existing eye trackers, regardless of the gaze estimation method employed, rely on a single-view framework, which employs either a single-camera setup [12], [14], [15], [25], or a multi-camera setup that is designed to acquire 3D info (stereo, depth) [5], [10], [22], [28] or to acquire high-resolution eye data using a pan-tilt unit [4], [7], [13]. On the other hand, the efficacy of the multi-camera systems that perform multi-view tracking has not adequately been investigated. In this regard, to the best of our knowledge, there exists only one previous effort. [29] proposed a two-camera setup mainly to obtain a wide observation area for a gaze-reactive signboard. Yet, the system was designed for a highly coarse gaze tracking, which achieved $\sim 11^\circ$ accuracy. Hence, we are the first to exploit a multi-camera setup for multi-view tracking so as to improve the estimation performance for high-accuracy eye tracking [19]. In this paper, we extend our previous work to also improve the tracking robustness under real-world conditions by investigating various multi-camera configurations as well as novel adaptive fusion mechanisms.

B. User Calibration

In addition to hardware setup calibration, user calibration has an important role in user experience and convenience. User calibration is required for modelling the person-specific parameters, which are crucial for the estimation bias correction. The calibration quality improves, to a certain extent, when the amount of calibration data increases. However, augmenting the data amount by increasing the number of calibration points could be tedious and thus harms the user experience. In this regard, the trade-off between the quality and convenience of the user calibration has been widely studied in the literature. Significant advancements have been made, for instance, better geometric eye models [21], [28], [30] and more effective bias correction models [14], [16], [18], [31] were developed, and implicit calibration methods were introduced [32], [33].

C. Head Movement Robustness

3D model-based methods are theoretically more tolerant to the changes in head pose and location due to explicit parametrization of person-specific eye parameters. Yet, in practice, they suffer from inaccuracy under large head movements. One of the main reasons is that most systems are faced with the dilemma of trading off between the head movement range and eye data resolution. In early efforts [4], [7], a wide field-of-view (FoV) stereo system was employed to allow free head movement as well as one or more narrow FoV stereo system to capture eye images with high resolution. These systems were mostly interconnected through a pan-tilt unit which mechanically reoriented the narrow FoV camera to the users' eye. Despite enabling high accuracy and certain head movement robustness, the use of a pan-tilt unit increased the setup complexity and cost. Consequently, in later efforts, researchers avoided such mechanical units and focused on introducing more robust models, which eliminated the need for the narrow FoV cameras. For instance, [6] introduced a method that used the centers of the pupil and at least two glints, which were estimated from the eye images captured by at least two cameras. Their system achieved $<1^\circ$ accuracy by tolerating head movements in a volume of $10 \times 8 \times 10 \text{ cm}^3$. In addition, [5] presented a single camera non-stereo system that employed the use of ray tracing rather than depth from focus. Their system allowed an accurate ($<1^\circ$) gaze estimation in a volume of $14 \times 12 \times 20 \text{ cm}^3$. Recently, [8] proposed a Kinect sensor-based technique, which used a parametrized iris model. They reported $1.4\text{--}2.7^\circ$ accuracy error under head movements in a volume of $20 \times 20 \times 8 \text{ cm}^3$.

Regression-based methods indirectly model the eye physiology, geometry, and optical properties. When the user moves away from the calibration position, the features non-linearly change, therefore, the calibration mapping becomes less accurate and the estimation accuracy degrades. To address this, multiple glints-based approaches have been suggested. [34] proposed to use a second light source, which permitted differentiation of head movement from eye rotation in the camera image. Using two glints as points of reference and exploiting spatial symmetries, they proposed a spatially dynamic calibration method to compensate for lateral head translation automatically. Later, a thorough review of polynomial-based regression methods using two glints was presented in [11]. They evaluated various models using different pupil-glint vectors and polynomial functions. In addition, [12] studied how binocular information can improve the accuracy and robustness against head movements for the polynomial based systems using one or two glints. Moreover, [23] suggested two calibration strategies to reduce the errors caused by head movements. The results of the experiments showed that both strategies achieved a reduction in error by a factor of two when the user's head was moved $\pm 6 \text{ cm}$ (depth) from the calibration position. From a different perspective, [10] proposed a stereo-based system that achieved an accuracy error of $\sim 2^\circ$ while allowing for a significantly greater working volume ($20 \times 20 \times 30 \text{ cm}^3$) without requiring a chinrest. They estimated the optical axis of the eye in 3D by directly applying triangulation techniques on the glints and pupil center. They

also suggested that 3D head pose information can be used to compensate for the bias caused by head movements. However, the main drawback was that a multi-camera fully-calibrated stereo setup was required to obtain 3D information.

Cross ratio-based methods are mainly sensitive to the depth movements. Various attempts have been made to enhance the depth movement tolerance. Most of these focused on adapting the user calibration to the changes in head movements. For instance, [15] proposed dynamic calibration correction and planarization of features, which achieved $\sim 0.5^\circ$ accuracy while tolerating up to $\pm 12.5 \text{ cm}$ depth changes. However, their system required high-resolution (640×480 pixels) eye images. Also, a chinrest was required to keep the users' eye within the camera's FoV and to fix the users' head pose and location during the experiments. [16] proposed a homography-based calibration modeling with a binocular fixation constraint to jointly estimate the homography matrix from both eyes. They reported $\sim 0.6^\circ$ using a much lower resolution while allowing for $\pm 5 \text{ cm}$ head movements. A potential drawback of their system was that the features from both eyes must be detected to compute a gaze output, which constrains the estimation availability due to the limited head pose allowance. Moreover, [17] proposed an adaptive homography calibration. They learned an offline-trained model on the simulated data by exploring the relationship between the estimation bias and varying head movements. They achieved promising results achieved both on the simulated ($\pm 25 \text{ cm}$) and real data ($\pm 10 \text{ cm}$). An important limitation in [16] and [17] is that they utilize a chinrest to keep the head pose fixed during their evaluation, similar to [15]. Although reporting performances using a chinrest may lead to more stable results, it causes the evaluations to discard the impact of variations in head pose. In addition, it significantly harms the user experience and would be impractical for real-world applications.

D. Eyewear (Glasses) Robustness

Considering that about 30% of young adults and more than half of elders in industrial nations need eyewear [35], any intolerance to glasses or contact lenses undoubtedly harms the user experience. Eyewear robustness, particularly to glasses, has been a challenging research problem since the reflection and refraction from glasses drastically obstruct the eye appearance and features. Since *appearance-based methods* [25]–[27] neither use light sources nor rely directly on the detection of individual gaze features, their performances are less affected by the glasses in comparison with *feature-based methods*, which require explicit solutions. Unfortunately, glasses robustness has largely been neglected by the majority of the previous work. There exists only a limited number of attempts to address the reflections and refraction on the glasses. [36] introduced a robust pupil detection method by leveraging the bright-pupil effect generated with a differential lighting scheme. He also suggested a method for eliminating the reflections appearing on the glasses. His method was successfully realized in [37] for monitoring driver vigilance. In addition, [7] proposed a dual illumination technique to avoid the reflections on the glasses. When a specular reflection was detected, the system deactivated the current illuminator and activated the alternative illuminator on the opposite side,

such that the reflection can be avoided. Moreover, a few other efforts (e.g., [28], [38]) proposed models to compensate for the refraction impact. They demonstrated that the gaze accuracy may differ more than 1° depending on whether refraction is accounted for. Recently, [39] simulated reflection and refraction of glasses to study their impacts in connection with pupil and glint detection. From a different perspective, this work addresses the robustness to glasses by focusing on generating and detecting more reliable gaze features. As the occlusion and distortion of features on an eye appearance depends on the relative positioning of a camera, light sources, and eye, we propose to perform multi-view tracking to obtain alternative eye appearances. Hence, the main benefit is that in case the glasses effects obstruct the features from certain views, they can still be recovered from alternative views.

III. PROPOSED METHODOLOGY

This section describes the details of the proposed multi-view eye tracking methodology. An overview of the methodology is illustrated in Fig. 1. It comprises of simultaneously operating independent single-camera systems, each of which consists of i) blink and gaze features detection (Section III-A) and ii) gaze estimation and user calibration (Section VIII-E) processes, as shown in Fig. 2. As the main contribution, gaze outputs obtained from each eye and camera are then fed into the proposed adaptive fusion mechanism to output an overall PoR, as described in Section III-C.

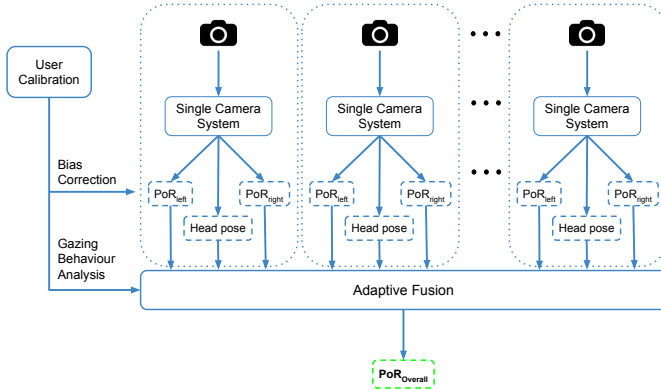


Fig. 1: Overview of the proposed multi-view framework.

A. Blink & Gaze Features Detection

Our methodology starts with eye localization, in which the existence of eyes is determined. In order to localize and track the eyes, we utilize a robust non-rigid face tracker based on supervised decent method (SDM) [40]. SDM method assumes that an accurate final face shape with 66 landmarks can be estimated with a cascade of regression models given an initial shape. Once the shape is fitted accurately, we extract eye regions by using the landmarks around eyes. Note that neither registration nor scaling is required, i.e., no particular eye region resolution is ensured. On the extracted eye regions, we perform blink detection followed by removal of glares on the glasses, if there exists any¹. We then continue with the feature detection, where the corneal reflections (glints) and pupil center are localized using image processing techniques.

¹Further details and illustrations on blink detection, glare removal, glint and pupil center detection are provided in the supplementary material.

For glint detection, we first perform histogram equalization to improve the contrast on input eye region. We then apply a thresholding to segment out the prospective glints. Here, we utilize spatial adaptive thresholding to take into account spatial variations in illumination. Instead of tuning a global threshold value, spatial adaptive thresholding applies different thresholds for small regions within the image, which leads to more robust results under varying illumination. Morphological opening and closing operations are then performed to get rid of the small blobs caused by noise. In the resulting binary image, we expect to find four blobs forming a trapezium since they emerge from the reflections of four LEDs located around the screen. Therefore, we perform connected component analysis to determine the candidate glints. If there are four or more candidate glints, we consider the shapes formed by any four-glints combination. The set of candidates whose convex hull has the highest match with a template shape representing the screen is considered as the final set of glints.

For pupil center detection, we follow a dark-pupil based approach rather than a bright-pupil based one due to its improved robustness to glasses and the variations in illumination and eye type¹. More specifically, we first perform bilateral filtering on input eye region with dark-pupil to smooth the pupil region while still keeping the edges (pupil to iris) sharp. We then equalize the histogram to enhance the contrast. We approximate the average intensity within the pupil by the surrounding regions of each glint and center of glints polygon. We then remove the glints by filling them with the average intensity. On the resulting image, we apply global thresholding by considering the average intensity within the pupil. We then invert the image to highlight the pupil blob. Nonetheless, a few other blobs, which are as dark as the pupil region, such as eye lashes, eye lids, shades, also remain in the binary image. To distinguish the actual pupil region from the noisy blobs, we perform morphological operations for the noise removal. Among the remaining candidate blobs, we determine the final pupil by considering the shape, size, and location of the blobs. Its center of gravity is then used as the pupil center feature.

B. Gaze Estimation & User Calibration

The proposed multi-view framework is independent of the gaze estimation algorithm used. Therefore, any gaze estimation technique described in Section II can be utilized within this framework. In this paper, we employ a *cross ratio-based* method due to its particular advantages, such as enabling high-accuracy using an uncalibrated and flexible setup. However, it can be replaced with any other method depending on the application requirements, desired accuracy and robustness.

The original method relies on the cross-ratio invariant of the projective space [13]. More specifically, four light sources are positioned around a screen to create glints on subject's cornea. The polygon formed by the glints on the cornea is the projection of the screen. Another projection takes place from the corneal plane to the image plane. As the virtual tangent plane on the cornea has the same planar projective transformation of the screen and image planes, the pupil center on the image plane corresponds to the PoR on the screen plane. Hence, the PoR can be computed by the equality of the

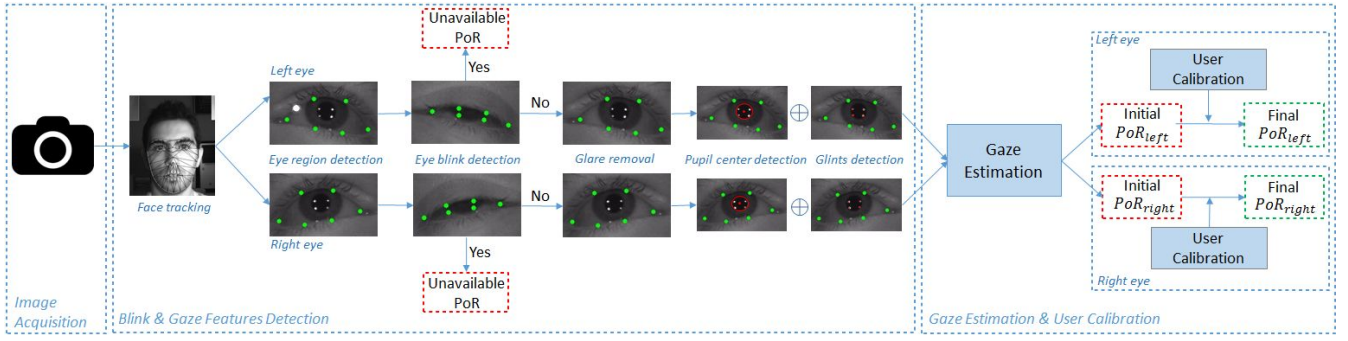


Fig. 2: Overview of a single-camera system, which comprises of two gaze tracking sensors, one for each eye.

cross-ratios on screen and camera image planes, as detailed in the supplementary material. Nevertheless, a user calibration is essential to compensate for the estimation bias caused by person-specific eye parameters, such as the angular offset between the visual and optical axis of the eyeball and the cornea radius and curvature as explained in more detail in [41]. The calibration is performed once, prior to the use of the system. The users are asked to look at N calibration points on the screen for K frames long. Person-specific bias correction, \mathcal{F} , can be learned by minimizing the distances between the estimated gaze positions and corresponding calibration points on the screen as follows:

$$\min \sum_i^N \sum_j^K \|\mathbf{P}_{i,j} - \mathcal{F}(\mathbf{Z}_{i,j})\|, \quad (1)$$

where $\mathbf{Z}_{i,j}$ and $\mathbf{P}_{i,j}$ are the estimated PoRs on the screen and the corresponding target calibration points, respectively.

Our methodology employs a regularized least-squares regression based calibration technique [18], [31]. The method has recently been shown to have better modeling and generalization capabilities than the state-of-the-art methods, owing to reduced model parameters. It enables to model the bias more effectively, particularly when the calibration data is limited in size and quality. Therefore, it facilitates tracking with low-resolution data and requires minimal user effort.

C. Adaptive Fusion Scheme

The proposed multi-view framework, which consists of individual single-camera trackers, is designed to empower a robust tracking under challenging conditions. Within this framework, each tracker simultaneously estimates the gaze for each eye (aka gaze sensor). In each frame, two distinct gaze outputs can be computed per camera. Consequently, in a multi-camera setup with C cameras, up to $2C$ gaze outputs can be generated per frame. The overall PoR can then be computed by the fusion of available gaze outputs obtained from all sensors. Here, we propose an adaptive fusion mechanism to effectively combine the gaze outputs towards achieving a higher overall estimation accuracy and robustness.

We have investigated several algorithms to perform the adaptive fusion. Among these, the most straightforward fusion is to simply average of all gaze outputs. Despite its simplicity, fusion by simple averaging in fact results in a significant improvement in estimation accuracy in comparison to any of the single-view trackers, particularly when the majority of the sensors produce reliable gaze outputs. In such cases, simple averaging provides a more accurate and consistent overall

estimation through smoothing out the arbitrary noise. On the other hand, under more challenging scenarios, in which a higher variance exists among available gaze outputs, fusion by simple averaging is far from an optimal fusion. To this effect, we propose to combine the available gaze outputs in a weighted manner, where the weights are determined according to the estimation reliability of each sensor. Here, there is several factors that affect the reliability, such as camera's viewing angle, gaze point location on the screen, eyewear effects, person-specific gaze behaviours. Fig. 3 shows sample eye appearances captured from different camera views when users gaze at different regions on the screen. While some views permit reliable gaze features, some others do not even contain any available features. The views capturing the best eye appearances continuously vary when users gaze at different regions on the screen. In addition, when users wear glasses, some reflection and refraction effects may occur on the glasses. When these effects distort or overlap with the features, the estimation becomes impossible from that particular view. On the other hand, as there exists simultaneously captured several other views, the features can still be recovered from some of these views. This, in fact, constitutes an important benefit of the multi-view approach in comparison to conventional single-view approach, employed by the majority of the previous work. Hence, an effective fusion that accounts for the estimation reliability of individual gaze outputs can significantly improve the overall estimation accuracy and robustness. The adaptive fusion is formulated as follows:

$$\begin{aligned} \mathbf{z}^* &= \sum_c \sum_e \mathbf{z}_c^e w_c^e, \\ \sum_c \sum_e w_c^e &= 1, \quad e \in \{L, R\}, \quad c \in \{1, 2, \dots, C\}, \end{aligned} \quad (2)$$

where \mathbf{z}^* is the overall PoR and w_c^R and w_c^L are the weights for the right and left eye's gaze outputs from the c^{th} camera, respectively. In case any of the gaze outputs cannot be computed at a frame, then the weight of the missing one is set to zero. We do not report an overall PoR in case there is no available gaze outputs for a given frame. To determine the weights, we propose two algorithms, namely, head pose-based fusion and person-specific gazing behaviour-based fusion:

1) *Head pose-based fusion*: As can be depicted in Fig. 3 and psycho-visually evidenced in [42], prior to the fixation, most users first perform head rotation to find the most comfortable viewing angle. Therefore, when users gaze at different target points, the eye appearances in cameras views continuously vary. Here, the estimation accuracy is strongly



Fig. 3: Example eye appearances from three different camera views: (left) left side camera, (middle) bottom camera and (right) right side camera while gazing at a stimulus point displayed on (top) upper-left and (bottom) upper-right region of the screen.

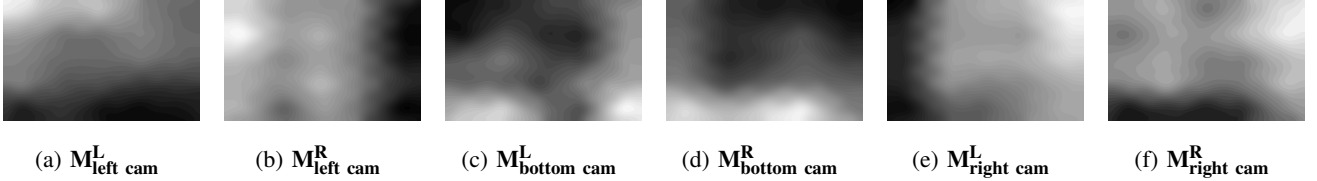


Fig. 4: Sample generated weight maps based on the calibration accuracy and gaze availability in a three-camera setup.

correlated with the quality of the eye appearance and gaze features, which relies on user's head pose relative to each camera view. For instance, when users gaze at the upper left corner of the screen, the left side camera system often generates more accurate estimations than the others. The main reason is obviously that the relative head pose is more frontal from left camera's view, and consequently the corresponding eye appearances facilitate a more reliable feature detection.

Hence, our first adaptive fusion relies on relative head pose angles estimated with respect to each camera. We assign the weights inversely proportional to the angles, as follows:

$$\lambda_c^e = \frac{\alpha_{max} - |\alpha_c^e|}{\alpha_{max}}, \quad (3)$$

$$w_c^e = \frac{\lambda_c^e}{\sum_c \sum_e \lambda_c^e}, \quad (4)$$

where α_c is the head pose yaw angle, α_{max} is the maximum angle allowed, e.g., 45° . We calculate head pose angles using the landmarks obtained by the face tracker and point distribution model [43]. Both eyes are assigned with the same weights. Normalization is then performed using Eq. (4) prior to fusion.

Note also that we investigated an alternative weighting approach in our previous effort [19]. Instead of calculating head pose angles, we first calculate an initial PoR using simple averaging. We then iteratively refine the initial estimation by weighting the cameras with respect to their distances to the estimations. Although this approach performs an effective fusion, it has two drawbacks: first, it requires camera locations to be known to compute the distances, and second, its performance is affected by the quality of the initial PoR. A poor initial PoR estimation leads to a less effective weighting.

2) *Gazing behaviour-based fusion*: Although head pose-based weighting works well for most users, still it does not take person-specific gazing behaviors into account, and consequently, it may experience a performance drop when a user has a particular gazing behaviour. For instance, although the majority of the users perform head rotation prior to fixation to have a comfortable viewing angle (frontal eyeball pose), some users do not perform any head movements but rather rotate their eye balls (non-frontal eyeball pose). In addition, head

pose-based approach weighs cameras rather than the eyes. However, some users' vision may rely more on one particular eye than the other due to eye dominance or a physiological reason (e.g., lazy eye, strabism). For such users, assigning equal weights to both eyes may result in a low estimation performance. Hence, we propose to determine person-specific weights for each eye independently through leveraging user's calibration data. During user calibration, we generate fusion weight maps in addition to learning the user calibration model. Once the weight maps are obtained, our algorithm performs a weighted averaging of individual gaze outputs as follows:

$$\mathbf{z}^* = \sum_c \sum_e \mathbf{z}_c^e \mathbf{M}_c^e(\mathbf{z}_c^e.x, \mathbf{z}_c^e.y), \quad (5)$$

$$\sum_c \sum_e \mathbf{M}_c^e(x,y) = 1, \quad e \in \{L, R\}, \quad c \in \{1, 2, \dots, C\},$$

where \mathbf{z}^* is the overall PoR, \mathbf{z}_c^e are initial gaze outputs estimated using simple averaging, and \mathbf{M}_c^R and \mathbf{M}_c^L are the weight maps of right and left eye of the c^{th} camera, respectively.

For generating the weight maps (\mathbf{M}_c^e), we extract various statistics that are relevant to the estimation reliability (e.g., accuracy, precision, availability, gain) from the calibration data. For instance, as perhaps the most relevant and effective indicator, we calculate the estimation accuracy of each sensor (eye) on each calibration point. If a sensor's calibration accuracy around a point is consistently higher than the others, that sensor's estimation performance during testing is expected to be more reliable around the same point. Thus, higher weights are assigned to the sensors with better calibration performances for certain regions. More specifically, to calculate the weighting indicators (e.g., $acc_{c,k}^e$) for each point, after learning the calibration model on the whole calibration data, we apply the learned model on the very same data. Then, we compute the aforementioned statistics on the calibrated samples, such as the accuracy by measuring how close the calibrated samples are to their corresponding target points. We perform this process for each calibration point of each sensor independently, and obtain 2C values for each calibration point. We then normalize these accuracy values to compute the

sensor weights ($w_{c,k}^e$) for each calibration point:

$$w_{c,k}^e = \frac{acc_{c,k}^e}{\sum_c \sum_e \sum_k acc_{c,k}^e}, \quad (6)$$

$$\mathbf{W}_c^e = \{w_{c,k}^e \mid e \in \{L, R\}, c \in \{1, 2, \dots, C\}, 1 \leq k \leq K\},$$

where K is the number of calibration points. Lastly, we interpolate and extrapolate the weight set (\mathbf{W}_c^e) over the whole screen to generate the weight maps (\mathbf{M}_c^e). Sample generated weight maps from a three-camera setup are shown in Fig. 4. In this paper, we use the estimation accuracy and availability statistics as the weighting indicators. Nevertheless, other alternatives can also be employed towards more robustly determining the sensor weights. For example, the estimation precision, which is the ability to reliably reproduce the same estimation for a target calibration point, or the histogram of the best performing sensor, which stores the information about how often each sensor achieves the best estimation for a target calibration point, could provide complementary evidence. We plan to investigate such alternative indicators in our future work. On the other hand, the main drawbacks of this method are: first, it may be sensitive to large head movements since the weights are estimated according to the calibration position, and second, an initial estimation using simple averaging is required to localize the weights on the generated maps.

IV. EVALUATION ON SIMULATED DATA

We conduct extensive simulations to primarily investigate and understand how the overall tracking performance is affected when the number of cameras is increased in various configurations. In real-world settings, the number of cameras to be employed for real-time eye tracking is limited due to certain factors, e.g., cost, data band-width, hardware constraints. Therefore, we start our evaluations on the simulated data to analyze the efficacy and limits of the proposed framework. We conduct various experiments on simulated data. We measure the tracking performance as the gaze estimation accuracy error and estimation availability on raw samples. Details of evaluation metrics are provided in the supplementary material.

A. Simulation Setup

Simulation data is generated using an open-source software framework developed by [44]. The simulator enables detailed modeling of different components of the hardware setup and an eye in 3D, and provides a realistic simulation framework. Nonetheless, there are still a few factors that are not currently simulated, such as non-spherical cornea shape, eyelid occlusions, eyewear effects, lens or sensor distortions.

To simulate the impact of increasing the number of cameras, we setup two configurations: i) single-view tracking by placing

multiple cameras densely at the bottom of a screen (*case 0*) and ii) multi-view tracking by placing them uniformly around a screen (*case 1*), as visualized in Fig. 5. We simulate an eye using the typical eye parameters listed in [28]. In addition, we simulate a similar environment that we have in the user experiments, i.e., 24-inch screen, 4 light sources, cameras with 1280×1024 pixels resolution, and lenses with 8mm focal length (diagonal FoV=58°) to allow for large head movements. We acquire calibration and test data using the simulated environment. For the calibration, we generated data when the eye gazes at 9 uniformly distributed target stimuli points on the screen, whereas for the test data acquisition, we randomly generate 18 test points to avoid reporting false test results due to overfitting on the calibration point locations. The test points are displayed in a 3×3 grid with 2 points per region to cover the whole screen. In addition, to simulate realistic test conditions, we alter the noise level to examine the impact of noise-free and noisy data. For each point, we collect 100 samples, and introduce uniformly distributed feature position errors with a maximum magnitude of 0.4 pixels per feature (noise level $\in \{0, 0.1, 0.2, 0.4\}$).

We perform simulations under two different scenarios, namely, *Stationary Head (SH)* and *Moving Head (MH)*. In *SH* scenario, the eye is located 60 cm to the screen and kept at the same position during the simulations. Whereas, in *MH* scenario, the eye location is changed along three directions, X, Y, and Z as shown in Fig. 8. In both scenarios, the calibration is performed at the default head position (0, 20, 60) cm.

B. Simulation Results on Stationary Head (SH) Scenario

In *SH* scenario, the main emphasis is given to the impact of increased number of cameras on estimation accuracy as there is no head movement. Fig. 6 shows the obtained results under various setup configurations while also altering the amount of feature detection noise to understand the theoretical and practical impact of setup configurations. In *case 0* (single-view tracking), when no noise is introduced, increasing the number of cameras, even up to 25 cameras, does not provide any estimation accuracy improvement (see Fig. 6a). Contrarily, when a significant amount of noise is introduced, the more cameras the system employs, the higher accuracies it achieves due to smoothing out the noisy outputs.

The simulation results shown in Fig. 6b indicate that not only the number of cameras, but also their configuration is crucial for improving the tracking performance. When there is no noise, a 3-camera multi-view setup (*case 1*) outperforms even a 25-camera single-view setup (*case 0*). In addition, the results suggest that when higher levels of noise are introduced (e.g., 0.4), the number of cameras has more impact than the configuration of cameras since more cameras can better filter the noise out. When the real-world noise level (~ 0.2) is introduced, the camera configuration is undoubtedly more effective than the number of cameras, such that multi-view configuration always outperforms single-view one when the same number of cameras is employed. Furthermore, Fig. 6c shows the comparison of non-adaptive and adaptive fusion mechanisms. The results indicate that the proposed adaptive mechanisms perform better than the simple averaging.

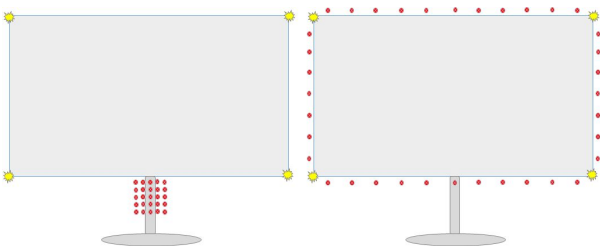


Fig. 5: Single-view (*case 0*) and multi-view (*case 1*) setups.

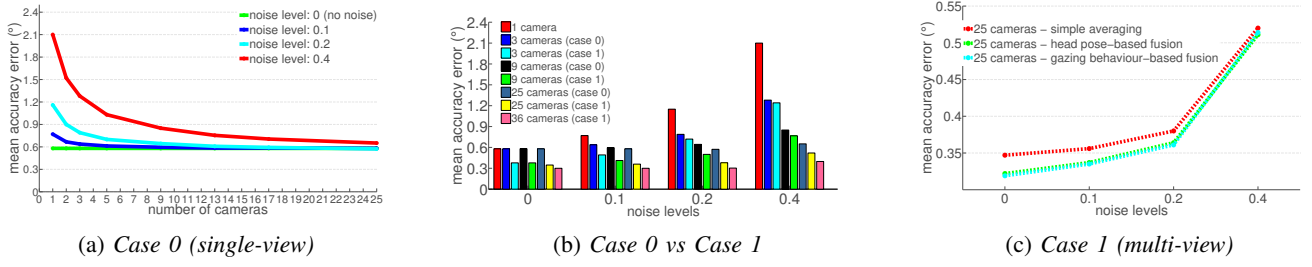


Fig. 6: SH scenario with varying feature detection noise levels. The impact of increasing number of cameras with (a) single-view and (b) multi-view setups, and (c) a comparison of the investigated fusion methods for multi-view tracking.

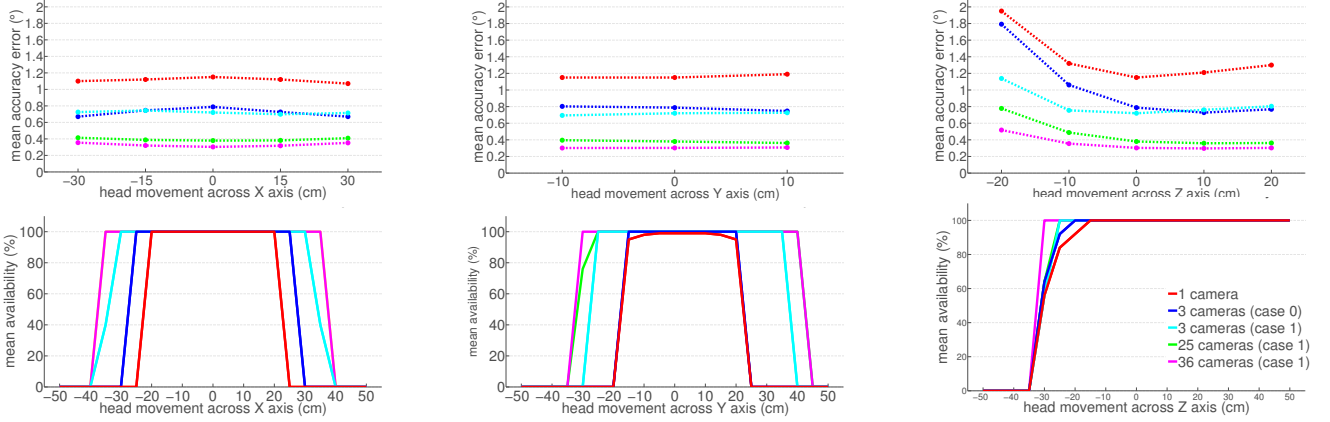


Fig. 7: MH scenario with a real-world (0.2) noise level. The impact of number of cameras and their configurations (*case 0* and 1) on the head movement robustness (top row) and gaze availability (bottom row) when user moves from the default calibration position (0, 20, 60) along X, Y, and Z directions. This figure best viewed in color. All subfigures have the same legend.

C. Simulation Results on Moving Head (MH) Scenario

In *MH* scenario, we examine the impact of single- and multi-view setups, particularly on the estimation availability and head movement robustness along X, Y, and Z directions. For this scenario, the virtual eye is calibrated at the default position (0, 20, 60) and real-world noise level (0.2) is introduced. The eye then is moved to various locations along three directions as shown in Fig. 8 and the tracking is performed in these locations using the learned calibration at the default position. As depicted in Fig. 7 (top row), the tracking is highly robust to head movements along X (horizontal) and Y (vertical) directions. In fact, even a single-camera configuration is highly tolerant owing to the gaze estimation itself as well as the user calibration technique employed [18]. In these cases, increasing the number of cameras simply enhances the

overall estimation accuracy. On the other hand, the robustness to head movements along Z axis (depth translations) is very challenging for *cross ratio*-based systems due to inaccurate user calibration. As the calibration is learned as an offset at a fixed head location, the learned offset does not sufficiently compensate for the bias when the user moves away from the calibrated position, especially along Z axis. Therefore, such movements cause a significant decay in estimation accuracy for a single-camera system. Nonetheless, as clearly depicted from the line slopes in Fig. 7 (top-right), multi-view setups (*case 1*) yields a significant tolerance compared to single-camera or single-view (*case 0*) setups. For instance, 3-camera multi-view configuration improves the accuracy by 43% and 35% in comparison to single-camera and 3-camera single-view configuration, respectively.

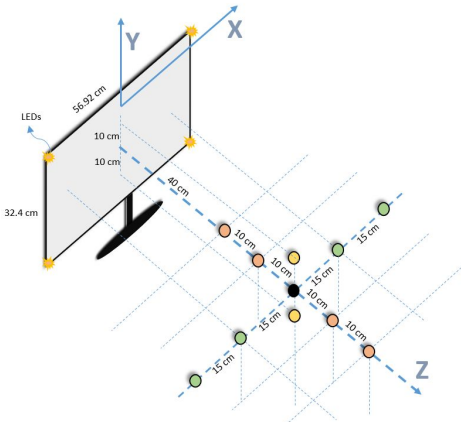


Fig. 8: Simulation setup. Calibration is at the black circle.

Furthermore, an important benefit of the multi-view tracking is the increased estimation availability. Fig. 7 (bottom row) demonstrates the impact of setup configurations on the gaze availability, in %, when the user moves along X, Y, and Z directions. The results clearly show that multi-view setups allow for significantly larger head movements (working volume) in all three directions in comparison to single-view setups. For instance, a 3-camera multi-view setup (*case 1*) provides an additional ± 15 cm and ± 10 cm head movement tolerance along X and Y directions, respectively. The reason is that each camera has a different FoV, and consequently, the system's overall FoV increases with the fusion of various FoVs. We also note that increasing the number of cameras many more (e.g., from 3 to 36) does not drastically improve the availability as their FoVs starts to overlap after a certain number of cameras.



Fig. 9: Prototype hardware setup.

V. EVALUATION ON USER EXPERIMENTS

This section describes the evaluation of our approach on real-world data obtained through user experiments.

A. Hardware Setup

Our prototype setup consists of three PointGrey Flea3 monochrome cameras, four groups of near-infrared (NIR) LEDs for the illumination, and a controller unit for the synchronization. Each camera has an image resolution of 1280×1024 , and is equipped with an 8 mm manual focus lens (diagonal FoV=58°). The cameras are installed on a frame around a 24-inch monitor as shown in Fig. 9. One camera is located slightly below the screen, whereas the other two are placed on the left and right sides of the screen. Note that the setup corresponds to the 3-camera multi-view *case 1* configuration as discussed in the simulations. In order to create the glints, 850nm-wavelength LEDs are placed on the corners of the monitor. A micro-controller is programmed to synchronize all cameras, so that the images are simultaneously captured from all cameras at 30 fps. In addition, we optimize the light emissions regarding the eye safety by synchronizing the cameras' shutters with the emission duration of LEDs.

B. Dataset & Experimental Protocol

A series of user experiments were conducted to comprehensively evaluate the proposed framework regarding the estimation accuracy, availability, robustness against head movements, varying illumination, eyewear, and between-subject variations. In total, 20 subjects, most of whom had no previous experience with any gaze tracking system, participated in our user experiments. 11 participants did not have any eyewear, while 5 and 4 participants wore glasses and contact lenses, respectively. The participants are from diverse origin. Therefore, eye shapes and appearances exhibit a large variability.

Each participant was asked to follow 8 different experiments as described in Table II. Experiment #2 being the default protocol, in the first three experiments, we analyzed the system's tolerance to varying illumination conditions by altering the ambient illumination, i.e., sunlight, darkness, indoor light. The remaining five experiments were designed to evaluate the system's robustness to head movements. Four of them were conventional experiments, in which the subjects were asked to move along X (horizontal) and Z (depth) axes. The remaining one stood for a novel scenario, in which the subjects were asked to continuously move their head while still fixating on the displayed gaze points. The goal

TABLE II: Experimental configurations.

Exp.	Lighting	Head (X, Z)		Experimental Variable
0	sunlight	0	60	illumination
1	darkness	0	60	illumination
2	indoor	0	60	illumination
3	indoor	0	60	continuous head movements (HM)
4	indoor	0	50	-10 cm HM along Z axis
5	indoor	0	70	+10 cm HM along Z axis
6	indoor	+15	60	+15 cm HM along X axis
7	indoor	-15	60	-15 cm HM along X axis

of this experiment was to analyze the system's sensitivity to continuous head movements, head pose changes, and slight head translations during the fixations. Such a scenario, in fact, occurs frequently in real-world scenarios, e.g., natural course of free-head gazing, listening music, talking on the phone. As our evaluation targeted natural human-computer interaction, we tried to collect the ground truth data as natural as possible for the subjects. For instance, we did not use a chinrest to keep the subject's head still and to keep the eye within the cameras' FoV to capture high resolution eye data, as frequently performed by previous work. In addition, the subjects were asked to gaze at the target stimuli points in a natural and comfortable way. As a result, the subjects had different head-pose and eye-pose characteristics, facial expressions, and heights (along Y axis) while gazing. Data acquisition and performance evaluations are done similar to the simulations described in Section IV-A. The default user-to-screen distance is set to 60 cm and user calibration is performed only at this distance. The learned calibration is then applied during testing for all configurations. Further details and statistics on user experiments as well as an example video (Exp #2 vs Exp #3) are provided in the supplementary material.

C. Results

The framework starts with face tracking on the captured frames, in which we extract eye regions of size $\sim 90 \times 50$ pixels. Feature detection is then performed to detect the pupil center and four glints. The size of the polygon formed by the glints is $\sim 9 \times 5$ pixels. Next, we apply *cross ratio-based* gaze estimation with the detected gaze features to calculate raw PoRs. We then apply the learned calibration models on raw gaze outputs to compensate for the person-specific bias. Lastly, calibrated PoRs obtained from each sensor are combined using the adaptive fusion mechanism to output an overall PoR. In the following subsections, we present and discuss the results of user experiments.

1) *Single-view vs Multi-view Tracking*: Our first analysis emphasizes on the benefits of multi-view tracking (*case 1*) over single-view tracking (*case 0*) as implemented by the

TABLE III: Comparison of single- and multi-view setups.

Setup configuration	Eye Data	Estimation (°)	(%)
Single-cam left eye only	1	1.4	77.6
Single-cam right eye only	1	1.35	69.6
Single-cam both eyes	max 2	1.25	93.4
Multi-cam (<i>case 0</i>)	max 6	1.04	97.2
Multi-cam (<i>case 1</i>) pose-based best cam selection	max 2	1.17	100
Multi-cam (<i>case 1</i>) simple averaging	max 6	0.89	100
Multi-cam (<i>case 1</i>) head pose-based fusion	max 6	0.76	100
Multi-cam (<i>case 1</i>) gazing behavior-based fusion	max 6	0.74	100

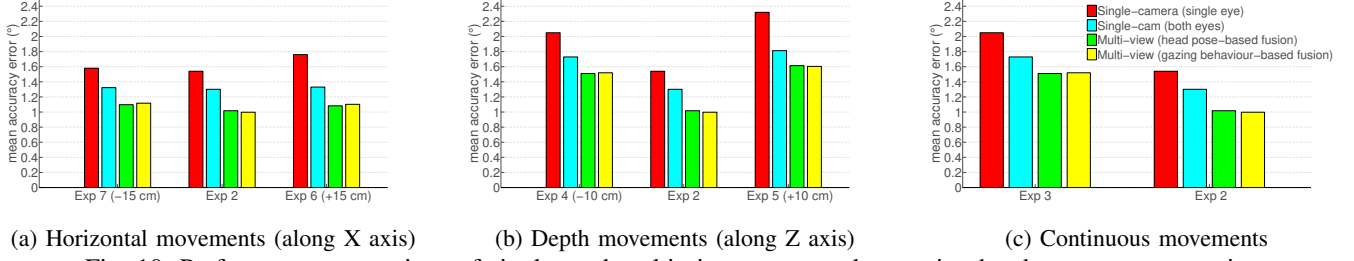


Fig. 10: Performance comparison of single- and multi-view setups under varying head movement scenarios.

majority of the existing trackers. In this regard, we conducted experiments on a subset of our subjects (3 subjects, one subject per eyewear category) using a single-camera, 3-camera single-view (*case 0*), and 3-camera multi-view (*case 1*) setups. Mean estimation accuracy errors and availabilities obtained using these setups on experiment #2 are shown in Table III. The results are clearly in line with the findings of the simulations (see Fig. 6), and demonstrate the efficacy of the proposed multi-view framework in terms of both estimation accuracy and availability. Firstly, significant accuracy improvements, by about 41% and 29%, are achieved using the proposed 3-camera multi-view setup in comparison to the conventional single-camera setup (using both eyes) and 3-camera single-view setup, respectively. In addition, the estimation availability is also increased. Yet, the availability analysis is more interesting when considering head movements and eyewear robustness in Sections V-C2 and V-C4. Furthermore, the results show the impacts of the adaptive fusion mechanisms. Although a simple averaging standalone achieves a significant performance improvement, employing the proposed adaptive fusion algorithms further enhances the accuracy.

2) *Head Movement Robustness*: To evaluate our framework's robustness to head movements, we analyze the results on experiments #2-7 on all subjects. Experiments #2, #6, and #7 account for the horizontal movements (along X axis), whereas experiments #2, #4 and #5 account for the depth movements (along Z axis). Note that vertical movements (along Y axis) are not explicitly experimented since the subjects, for their convenience, were asked to freely adjust their heights. Moreover, we introduced a new experimental scenario (experiment #3), in which the users were asked to perform continuous head pose/location changes while still fixating on the target points. The purpose of this experiment is to measure the system's sensitivity to sudden arbitrary changes during the user interaction, which may frequently occur in real-world conditions. Fig. 10 illustrates the results achieved on these experiments and their cross comparisons.

For horizontal head movement robustness, the results (Fig. 10a) are highly in line with the simulation results (Fig. 7), such that the system is highly tolerant (1° vs 1.1°) to head movements along X axis up to ± 15 cm movements. On the other hand, along Z axis (depth translations), the results partially differ from the simulation results. In simulations (Fig. 7), the estimation accuracy is shown to be negatively affected by the depth movements. The same result holds for the user experiments. However, we also observe that the system's performance gets worse when users move away from the screen, which contradicts the simulation results. In

fact, the main reason relates to the current hardware setup, which employs manual focus lenses. Despite the aperture adjustments to obtain a larger depth-of-field, the defocus is still observed when user's depth varies from the default position. This causes blurry appearances, and consequently less precisely detected features. In addition, the eye image resolution gets significantly lower when the user moves away from the camera, which causes the features to be detected less accurately. Yet, in overall, the multi-view framework provides more robustness, by about 25% in accuracy and 10% in availability, to depth translations compared to the single-camera system. Furthermore, continuous head movements results are shown in Fig. 10c. The results indicate that the framework, as expected, experiences an accuracy drop, yet it continues to output PoRs with an acceptable accuracy ($\sim 1.4^\circ$) under such a challenging scenario. As this new experimental scenario constitutes an essential use case in real-world eye tracking, we recommend future efforts to consider it in their evaluations.

3) *Illumination Robustness*: Fig. 11 illustrates the proposed framework's robustness under sunlight, darkness, and indoor lighting. The results indicate that ambient illumination variations do not significantly influence the estimation performance. As the suggested framework operates under active (NIR) illumination, the system is implicitly more robust to illumination variations than natural light-based systems. For our system, the robustness is in practice more related to how robust the employed feature detection algorithms are to the changes in features when the illumination varies (Fig. 12). In this respect,

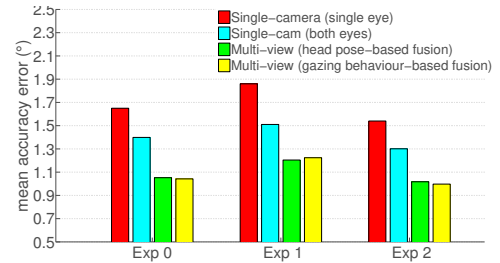


Fig. 11: Performance comparison under varying illumination.

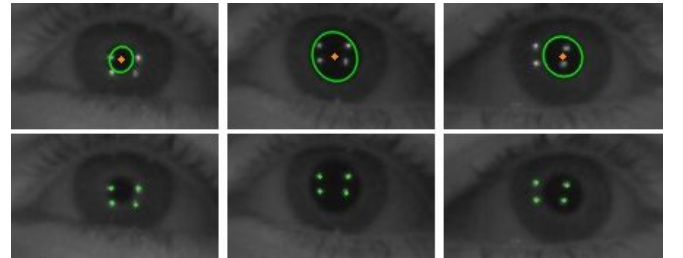


Fig. 12: Sample appearances of eye and gaze features (glints and pupil) under varying illumination conditions: (left) sunlight, (center) darkness, and (right) indoor lighting.



Fig. 13: Sample impacts of glasses on eye appearance.

we proposed illumination-robust feature detection algorithms, as described in detail in the supplementary material. We also note that our results under indoor lighting slightly outperforms the others because the feature detection is mainly optimized for this scenario.

4) *Eyewear Robustness*: This is undoubtedly one of the most challenging issues in eye tracking. Unfortunately, it has been neglected by the great majority of the previous efforts. The main challenges stem from the reflection and refraction effects on the glasses, which can significantly affect the tracking performance. Example glasses impacts on eye appearance, such as distorted features due to the refraction and coating, lost features due to the reflection, challenging feature detection due to multiple reflections, which were encountered during the user experiments can be seen in Fig. 13. As some of the impacts are unrecoverable, conventional single-view approaches are likely to fail under such circumstances. On the other hand, the proposed multi-view approach leverages various eye appearances per frame, in such a way to more reliably detect the features from various views.

We evaluate the efficacy of our proposed method with two separate analysis. First, we categorize the subjects into 4 groups according to their eyewear and vision quality such as the ones who wear glasses, who wear contact lenses, who do not wear glasses, and who have perfect vision. Fig. 14 shows the performance comparison across these groups. The results clearly depict the improvements achieved using the multi-view setup for both the generic scenario (experiment #2) and over all scenarios (experiments #0-#7). Among all groups, the best performance ($\sim 0.8^\circ$) is obtained on the subjects with perfect vision (6 subjects) and contact lenses (4 subjects). For the subjects who do not wear glasses (15 subjects), a small accuracy drop is observed. The reason relates to these subjects' lower quality (non-sharp) vision. Lastly, the subjects with glasses (5 subjects) achieves a lower accuracy (1.38° with 91.9% availability) in comparison with the other groups. However, the performance improvement, by about 0.6° and 10%, compared to the single-camera setup highlights the benefits of the multi-view approach.

Furthermore, to eliminate between-subject variations, we compare the performances on the same subject, who completed the user experiments firstly by wearing glasses and then once

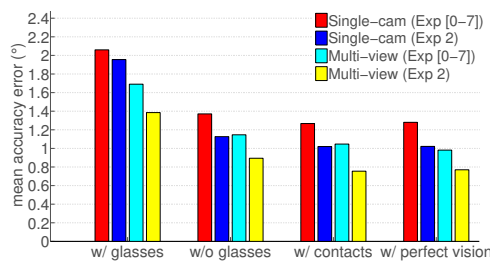


Fig. 14: Performance comparison of varying eyewear groups.

TABLE IV: Performance comparison on the same subject.

Eyewear	Single-cam view				Multi-view			
	Exp 2 (°)	(%)	Exp [0-7] (°)	(%)	Exp 2 (°)	(%)	Exp [0-7] (°)	(%)
Contacts	0.99	96.1	1.18	95.1	0.76	100	0.97	99.9
Glasses	2.1	84	2.31	82	1.08	100	1.53	99

again by wearing contact lenses. The results shown in Table IV shows the efficacy of the multi-view system over the single-view one. For glasses, it provides a substantial improvement in accuracy by about 50% and 40% for the generic scenario and all scenarios, respectively. In addition, it brings $\sim 17\%$ enhancement in estimation availability. For contact lenses, single-camera system standalone yields a high accuracy and availability. Yet, a multi-view system further enhances the accuracy and availability.

VI. DISCUSSION

Future directions in eye tracking research, towards becoming a pervasive technology, should not only focus on achieving high estimation accuracies, but also on having robustness against real-world settings such as natural head pose changes, large head movements, varying illumination conditions, use of eyewear, and between-subject eye type variations. Besides, having a convenient user calibration, flexible hardware setup, minimal setup calibration, low complexity, and low cost should be taken into consideration as important evaluation criteria. In this regard, in Section II, we describe various eye tracking techniques, analyze their pros and cons with respect to each other, and discuss whether they satisfy some of the aforementioned criteria. Therefore, the best, in other words, the most appropriate, approach depends on the application requirements. In this work, we mainly target eye tracking scenarios that require high estimation accuracy ($\sim 1^\circ$) and robustness, e.g., gaze-based controlling, typing and navigation. To achieve our accuracy and robustness goals, we design a novel multi-camera framework, which tracks users' gaze simultaneously from various views, and then combines the acquired gaze information from all sensors using an adaptive fusion mechanism to output an overall PoR. In comparison with conventional single-view approaches, multi-view tracking enables a more reliable gaze features detection even under challenging scenarios. In addition, owing to the proposed adaptive fusion mechanisms, the framework achieves high accuracies and robustness under real-world conditions.

A comparison of previous work in various aspects such as hardware setup and calibration requirements, accuracy, robustness, and working volume, is given in Table V. Since the majority of existing efforts requires particular hardware and system setups, e.g., additional light sources, setup calibration, use of 3D or depth information, we could not reproduce and validate the reported performances for all of them. Instead, for these, we reported the performances directly from the corresponding references. Thus, although a direct numerical comparison would not be completely fair, the provided information can still help us to make the following inferences. First of all, we observe that the popularity of *appearance-based* methods, which have lower hardware and calibration requirements, have been increasing recently in parallel with the recent advancements in machine learning, e.g., convolu-

Method		Hardware Setup			Accuracy			Robustness				FoV
		Cam(s)	Light(s)	Calib.	SH(°)	MH(°)	Eye Data	HP	Head Movement	Eyewear	Illum.	FL
Appearance	Zhang et al (2015) [25]	1	-	-	6.3 ¹	?	Both	Free	?	✓	✓	?
	Wood et al (2016) [27]	1	-	-	9.95 ²	?	?	Free	?	✓	✓	?
	Lu et al (2015) [24]	1	-	-	2.5	9.65	Single	Free	(40 x ? x ?)	-	-	?
	Mora & Odobez (2016) [45]	1+Kinect	5	pre	1.9 ³	3.5	Both	Free	?	-	-	6.1
	Krafka et al (2016) [26]	1	-	-	~3.5 ⁴	?	Both	Free	?	✓	✓	?
3D Model	Beymer & Flickner (2003) [4]	4*	2	fully	~0.6	-	Single	Free	Limited	-	-	4.8
	Hennessey et al (2006) [5]	1+1	3	fully	~1	<1	Single	Free	(14 x 12 x 20)	-	-	32
	Guestrin & Eizenman (2007) [6]	2	4	fully	-	~1	Single	Free	(10 x 8 x 10)	-	-	35
	Park (2007) [7]	1+2*	4	fully	-	~1	Both	Free	(? x ? x 20)	✓	-	?
	Lai et al (2015) [22]	2	2	fully	-	~1	Single	Free	(10 x 5 x 10)	-	-	37
	Sun et al (2015) [8]	Kinect	?	pre	~1.5	~2	Single	Free	(20 x 20 x 8)	-	-	6.1
Regression	Zhu & Ji (2007) [10]	2	2	fully	~1.1	~1.8	Single	Free	(20 x 20 x 30)	-	-	?
	Cerrolaza et al (2008) [11]	1	2	-	~1	~1	Single	Fixed	(0 x 0 x 10)	-	-	35
	Sesma-sanchez et al (2012) [12]	1	2	-	~1	~1	Both	Fixed	(0 x 0 x 6)	-	-	35
	Cerrolaza et al (2012) [23]	1	2	-	~0.9	~1.3	Single	Fixed	(0 x 0 x 12)	-	-	16
Cross ratio	Yoo & Chung (2005) [13]	1+1*	4+1	-	~1.6	-	Single	Free	Limited	-	-	?
	Hansen et al (2010) [14]	1	4	-	~1	-	Single	Free	Limited	-	-	?
	Coutinho & Morimoto (2013) [15]	1	4+1	-	~0.4	~0.5	Single	Fixed	(25 x ? x 25)	-	-	> 35
	Zhang & Cai (2014) [16]	1	8	-	~0.4	~0.6	Both	Fixed	(10 x ? x 20)	-	-	13
	Huang et al (2014) [17]	1	8	-	~0.8	~1.6	Single	Fixed	(? x ? x 20)	-	-	13
	Arar et al (2015) [19] (multi-view)	3	4+1	-	0.86	-	Both	Free	Limited	-	-	12 ⁵
	Proposed multi-view framework	3	4	-	0.99	1.27	Both	Free	(30 x ? x 20)	✓	✓	8 ⁵

TABLE V: Comparison of existing eye tracking systems. In "Cam(s)" column, * indicates that a pan-tilt unit is employed. "Calib." column indicates whether explicit camera and scene geometry calibrations are required: "fully" means both are required, "pre" means the sensor is pre-calibrated. In "Accuracy", "SH" and "MH" correspond to stable and moving head scenarios, respectively. The results refer to, unless stated otherwise, person-specific scenarios on within-dataset evaluations. "HP" column indicates whether users' head pose were fixed, e.g., using a chinrest. In "FoV" column, the systems' working volume is presented by "FL", focal length in mm. The smaller the focal length, the larger the FoV.

tional neural networks (CNNs), and in the synthesizing and rendering technology. Despite the fact that their accuracies and head movement tolerances are still not comparable to those of *feature-based* methods, their potential is likely to be exploited in the foreseeable future. On the other hand, even though *feature-based* methods outperform *appearance-based*, the bothersome hardware requirements, e.g., NIR cameras and light sources, remain an important concern. The setup complexity is especially high for *3D model-based* systems, such that fully-calibrated setups consisting of multiple cameras or a Kinect-like sensor are required for accurate 3D modelling. *Cross ratio-based* systems and most of *regression-based* systems have an important advantage over *3D model-based* ones. They require uncalibrated setups and less complex (2D) eye models, yet their accuracies are competitive with *3D model-based* systems. Among these, it is also clear that there is an accuracy gap between fixed-head (using a chinrest) and free-head eye tracking since they rely on approximated models.

Moreover, the results indicate that tracking performances significantly benefit from high-resolution eye data. For example, [15] reports an impressive accuracy, about 0.5°, under large head movements through planarization of gaze features. Nonetheless, their system required eye resolution of 640×480 pixels, that is 7-fold of ours. They capture eye data using a narrow FoV lens, and a chinrest was required to keep users' eye within the FoV of the camera. In addition, [17] and [16] proposed two alternative methods that are highly effective to compensate for the head movements, while requiring relatively lower resolution eye data, i.e., 13-mm focal lenses were used. However, similar to [15], they both utilized a chinrest during their evaluation. Since using a chinrest is unnatural for users and represents an unrealistic tracking scenario, it remains an important limitation of their evaluations. On the contrary, our methodology allows for not only head transla-

tions but also head rotations while requiring lower resolution eye data (~90×50 pixels) captured using 8-mm lenses. Lower resolution data naturally results in a lower accuracy, yet, the proposed adaptive fusion mechanism successfully closes the accuracy gap by effectively combining the gaze outputs obtained by multiple sensors. Besides, our system accounts for eyewear and illumination robustness, which have largely been neglected by the majority of the previous efforts.

As depicted from Table V, the proposed multi-view approach and implemented prototype system achieves a competitive accuracy while offering more robustness to aforementioned real-world conditions. Still, further improvements on accuracy, robustness or setup complexity can be achieved through certain hardware and software modifications. For instance, explicit head movement compensation techniques, such as learning an adaptive homography from simulated data [17] or planarization of features [15], can be employed to further improve the head movement robustness. In addition, as utilized by most commercial eye trackers, certain hardware solutions, e.g., auto-focus lenses or smart dynamic illumination techniques, can greatly enhance the estimation accuracy and availability. On the other hand, as the multi-view framework is independent of the gaze estimation method used, alternative gaze estimation methods can also be integrated according to the application requirements. Even though *cross ratio-based* method is suggested due to its particular advantages mentioned in Section II, an *appearance (CNN)-based* method (e.g., [25], [26]) can be utilized to lower the setup complexity, or an *3D model-based* method can be implemented to achieve even higher accuracies. Besides, the number of cameras and their

¹Person-independent within-dataset evaluation on MPIIGaze dataset [25].

²Person-independent cross-dataset evaluation on MPIIGaze dataset [25].

³Person-specific within-dataset evaluation on Eyediap dataset [46].

⁴Person-specific within-dataset evaluation on GazeCapture dataset [26].

⁵Single camera property. Multi-view setup has a significantly larger FoV.

configuration can be alternated according to the application scenario without requiring further system adjustments, particularly for uncalibrated settings. For instance, the current prototype can easily be configured to work under challenging tracking scenarios, such as in-car driving scenarios, children's eye tracking, or customized eye trackers for disabled people.

VII. CONCLUSIONS

This paper presents a novel multi-view eye tracking framework to revisit the robustness concerns in eye tracking, particularly to head movements and glasses. Instead of computing the user gaze from a single view as performed by the previous work, leveraging multiple eye appearances simultaneously acquired from various views provides with enhanced estimation accuracy and robustness under challenging real-world conditions. The main advantage of the multi-view approach is that for each frame, we calculate multiple gaze outputs using the features extracted from various eye appearances. This enables to extract the features more reliably even under challenging conditions, where they are obstructed in the conventional single-camera view. Under large head movements and use of glasses, our evaluations show that the proposed approach improves the tracking performance of a single-camera setup by about 20% ($0.2\text{--}0.6^\circ$) in estimation accuracy and 10-20% in estimation availability. The results also demonstrate that our approach is highly tolerant to illumination and between-subject eye type variations. In addition to the improved robustness to challenging conditions, the system's overall accuracy greatly benefits from the multi-view setup under normal conditions. The proposed methodology provides by about 30% improvement in accuracy, owing to the adaptive fusion mechanisms, which account for the reliability of estimations determined from user's general gazing behavior and momentary head poses with respect to each camera. The current implementation runs at 30 fps and achieves $\sim 1^\circ$ estimation accuracy error and nearly 100% estimation availability under challenging experimental scenarios, which makes it appropriate for high-accuracy demanding application scenarios.

REFERENCES

- [1] G. Underwood, *Cognitive processes in eye guidance*. Oxford Pr., 2005.
- [2] A. T. Duchowski, *Eye tracking methodology*. Springer, 2007.
- [3] D. W. Hansen and Q. Ji, "In the eye of the beholder: a survey of models for eyes and gaze," *PAMI*, vol. 32, no. 3, pp. 478–500, 2010.
- [4] D. Beymer and M. Flickner, "Eye gaze tracking using an active stereo head," in *CVPR*, 2003, pp. 451–458.
- [5] C. Hennessey, B. Noureddin, and P. Lawrence, "A single camera eye-gaze tracking system with free head motion," *Measurement*, 2006.
- [6] E. D. Guestrin and M. Eizenman, "Remote Point-of-Gaze Estimation with Free Head Movements Requiring a Single-Point Calibration," in *Proc. Int. Conf. Eng. Med. Biol. Soc.*, 2007, pp. 4556–4560.
- [7] K. R. Park, "A real-time gaze position estimation method based on a 3-D eye model," *TSMC Part B*, vol. 37, no. 1, pp. 199–212, 2007.
- [8] L. Sun, Z. Liu, and M. T. Sun, "Real time gaze estimation with a consumer depth camera," *Inf. Sci. (Ny)*, vol. 320, pp. 346–360, 2015.
- [9] Z. Zhu, Q. Ji, and K. P. Bennett, "Nonlinear eye gaze mapping function estimation via support vector regression," in *ICPR*, 2006, pp. 1132–1135.
- [10] Z. Zhu and Q. Ji, "Novel Eye Gaze Tracking Techniques Under Natural Head Movement," *TBE*, vol. 54, no. 12, 2007.
- [11] J. J. Cerrolaza, A. Villanueva, and R. Cabeza, "Taxonomic study of polynomial regressions applied to the calibration of video-oculographic systems," in *ETRA*, 2008.
- [12] L. Sesma-sanchez, A. Villanueva, and R. Cabeza, "Gaze Estimation Interpolation Methods Based on Binocular Data," *TBE*, vol. 59, no. 8, pp. 2235–2243, 2012.
- [13] D. H. Yoo and M. J. Chung, "A novel non-intrusive eye gaze estimation using cross-ratio under large head motion," *CVIU*, vol. 98, no. 1, 2005.
- [14] D. Hansen, J. Agustin, and A. Villanueva, "Homography normalization for robust gaze estimation in uncalibrated setups," in *ETRA*, 2010.
- [15] F. L. Coutinho and C. Morimoto, "Improving head movement tolerance of cross-ratio based eye trackers," *IJCV*, vol. 101, no. 3, 2013.
- [16] Z. Zhang and Q. Cai, "Improving cross-ratio-based eye tracking techniques by leveraging binocular fixation constraint," in *ETRA*, 2014.
- [17] J.-B. Huang, Q. Cai, Z. Liu, N. Ahuja, and Z. Zhang, "Towards accurate and robust cross-ratio based gaze trackers through learning from simulation," in *ETRA*, 2014, pp. 75–82.
- [18] N. M. Arar, H. Gao, and J. P. Thiran, "A regression-based user calibration framework for real-time gaze estimation," *TCSVT*, 2016.
- [19] —, "Robust gaze estimation based on adaptive fusion of multiple cameras," in *IEEE Int. Conf. Aut. Face & Gesture Recogn. (FG)*, 2015.
- [20] J. J. Kang, E. D. Guestrin, W. J. Maclean, and M. Eizenman, "Simplifying the cross-ratios method of point-of-gaze estimation," in *Can. Med. Biol. Eng. Conf.*, 2007.
- [21] A. Villanueva and R. Cabeza, "A novel gaze estimation system with one calibration point," *TSMC Part B*, vol. 38, no. 4, pp. 1123–1138, 2008.
- [22] C. C. Lai, S. W. Shih, and Y. P. Hung, "Hybrid method for 3-D gaze tracking using glint and contour features," *TCSVT*, vol. 25, no. 1, 2015.
- [23] J. Cerrolaza, A. Villanueva, M. Villanueva, and R. Cabeza, "Error characterization compensation in eye tracking systems," in *ETRA*, 2012.
- [24] F. Lu, Y. Sugano, T. Okabe, and Y. Sato, "Gaze Estimation From Eye Appearance: A Head Pose-Free Method via Eye Image Synthesis," *TIP*, vol. 24, no. 11, pp. 3680–3693, 2015.
- [25] X. Zhang, Y. Sugano, M. Fritz, and A. Bulling, "Appearance-based gaze estimation in the wild," in *CVPR*, 2015, pp. 4511–4520.
- [26] K. Krafka, A. Khosla, P. Kellnhöfer, H. Kannan, S. Bhandarkar, Matusik, and A. Torralba, "Eye tracking for everyone," in *CVPR*, 2016.
- [27] E. Wood, T. Baltrušaitis, L.-P. Morency, P. Robinson, and A. Bulling, "Learning an appearance-based gaze estimator from one million synthesised images," in *ETRA*, 2016, pp. 131–138.
- [28] E. Guestrin and M. Eizenman, "General Theory of Remote Gaze Estimation Using the Pupil Center and Corneal Reflections," *TBE*, vol. 53, no. 6, pp. 1124–1133, jun 2006.
- [29] A. Utsumi, K. Okamoto, N. Hagita, and K. Takahashi, "Gaze tracking in wide area using multiple camera observations," in *ETRA*, 2012.
- [30] T. Nagamatsu, R. Sugano, Y. Iwamoto, J. Kamahara, and N. Tanaka, "User-calibration-free gaze estimation method using a binocular 3D eye model," *IEICE Trans. Inf. Syst.*, vol. E94-D, no. 9, pp. 1817–1829, 2011.
- [31] N. M. Arar, H. Gao, and J. P. Thiran, "Towards convenient calibration for cross-ratio based gaze estimation," in *WACV*, 2015, pp. 642–648.
- [32] L. Sun, M. Song, Z. Liu, and M. Sun, "Real-time gaze estimation with online calibration," *IEEE Multimedia*, vol. 21, no. 4, pp. 28–37, 2014.
- [33] J. Chen and Q. Ji, "A probabilistic approach to online eye gaze tracking without explicit personal calibration," *TIP*, vol. 24, no. 3, 2015.
- [34] K. White, T. Hutchinson, and J. Carley, "Spatially Dynamic Calibration of an Eye-Tracking System," *TSMC*, vol. 23, no. 4, pp. 1162–1168, 1993.
- [35] F. Schaeffel, "Myopia: The Importance of Seeing Fine Detail," *Curr. Biol.*, vol. 16, no. 7, pp. 257–259, apr 2006.
- [36] Y. Ebisawa, "Improved video-based eye-gaze detection method," *IEEE Trans. Instrum. Meas.*, vol. 47, no. 4, pp. 948–955, 1998.
- [37] Q. Ji and X. Yang, "Real-time eye, gaze, and face pose tracking for monitoring driver vigilance," *Real-Time Imaging*, vol. 8, no. 5, 2002.
- [38] A. Villanueva and R. Cabeza, "Models for gaze tracking systems," *Eurasip J. Image Video Process.*, vol. 2007, pp. 1–16, 2007.
- [39] T. C. Kübler, T. Rittig, E. Kasneci, J. Ungewiss, and C. Krauss, "Rendering refraction and reflection of eyeglasses for synthetic eye tracker images," in *ETRA*, 2016, pp. 143–146.
- [40] X. Xiong and F. De la Torre, "Supervised Descent Method and Its Applications to Face Alignment," in *CVPR*, 2013, pp. 532–539.
- [41] J. Kang, M. Eizenman, E. Guestrin, and E. Eizenman, "Investigation of the Cross-Ratios Method for Point-of-Gaze Estimation," *TBE*, vol. 55, no. 9, pp. 2293–2302, sep 2008.
- [42] W. H. Zangemeister and L. Stark, "Types of gaze movement: variable interactions of eye and head movements," *Experimental neurology*, vol. 77, no. 3, pp. 563–77, 1982.
- [43] J. M. Saraghi, S. Lucey, and J. F. Cohn, "Face alignment through subspace constrained mean-shifts," in *ICCV*, 2009, pp. 1034–1041.
- [44] M. Böhme, M. Dorr, M. Graw, T. Martinetz, and E. Barth, "A software framework for simulating eye trackers," in *ETRA*, 2008, p. 251.
- [45] K. A. Mora and J.-M. Odobez, "Gaze Estimation in the 3D Space Using RGB-D Sensors," *IJCV*, vol. 118, no. 2, pp. 194–216, jun 2016.
- [46] K. A. Mora and J.-M. Odobez, "Geometric generative gaze estimation (G3E) for remote RGB-D cameras," in *CVPR*, 2014, pp. 1773–1780.

- [47] K. Nguyen, C. Wagner, D. Koons, and M. Flickner, "Differences in the infrared bright pupil response of human eyes," in *ETRA*, 2002, p. 133.
- [48] D. H. Yoo, J. H. Kim, B. R. Lee, and M. J. Chung, "Non-contact eye gaze tracking system by mapping of corneal reflections," in *IEEE Int. Conf. Aut. Face & Gesture Recogn. (FG)*, 2002, pp. 101–106.
- [49] A. Fakhro, H. W. Yim, Y. K. Kim, and A. H. Nguyen, "The evolution of looks and expectations of asian eyelid and eye appearance," *Seminars in Plastic Surgery*, vol. 29, no. 3, pp. 135–144, 2015.
- [50] K. Kiranantawat, J. Suhk, and A. Nguyen, "The asian eyelid: Relevant anatomy," *Seminars in Plastic Surgery*, vol. 29, no. 3, pp. 158–164, 2015.
- [51] S. Ren, X. Cao, Y. Wei, and J. Sun, "Face Alignment at 3000 FPS via Regressing Local Binary Features," in *2014 IEEE Conf. Comput. Vis. Pattern Recognit.*, jun 2014, pp. 1685–1692.
- [52] V. Kazemi and J. Sullivan, "One millisecond face alignment with an ensemble of regression trees," in *2014 IEEE Conf. Comput. Vis. Pattern Recognit.*, jun 2014, pp. 1867–1874.

Supplemental Information: Robust Real-Time Multi-View Eye Tracking

VIII. FURTHER DETAILS ON THE PROPOSED METHODOLOGY

This section presents additional details of the proposed multi-view eye tracking methodology, which were not included in the paper due to page limitations.

A. Blink Detection

In order to determine whether there is any eye blink, we analyze the positioning of the landmarks around the eyes. More specifically, we measure the vertical opening (height) of both eyes relative to the eye width. As illustrated in Fig. S15, if the average of the ratio of eye height to eye width for both eyes is significantly lower (< 0.15) than the open eye form (~ 0.5), we determine that a natural eye blink occurs. Once an eye blink is detected on a frame, the system skips the following processes as no gaze features are available or reliable. Therefore, no gaze output is generated for the frame. Since an eye blink is on average completed within 100 to 200 milliseconds after the peak closure of eyelids, the system does not also output any PoR for the corresponding number of frames upon detection of an eye blink. On the other hand, if the system misses an eye blink, the system proceeds with the feature detection, and naturally no features are detected as the pupil area is not visible due to the blink. Hence, the performance of the system does not depend on the blink detection process. The blink detection process is rather used for computational efficiency as well as providing additional information.

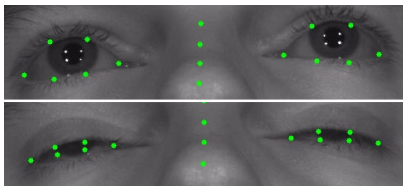


Fig. 15: The positioning of facial landmarks in case of (top) no eye blink, (bottom) an eye closure during a blink.

B. Glare Removal

Glare removal can be considered as a preprocessing of the input eye image to ease the actual feature detection. It mainly aims to clear out the noisy blobs, particularly the specular reflections caused by the eye glasses reflections, which might confuse the glints and pupil detectors. Since the glares on the eye glasses have considerably higher intensities than the rest, we employed well-known image processing techniques for the removal of the glare(s). More specifically, we firstly perform a global thresholding operation, followed by a few morphological erosion and dilation operations to obtain the binary mask of the detected glare. Then, we clean the detected glares by filling them up with the approximated average intensity calculated around the glares. A sample impact of the glare removal process is shown in Fig. S16. In the resulting eye image, the gaze features can more reliably be detected when the patches do not overlap with them.

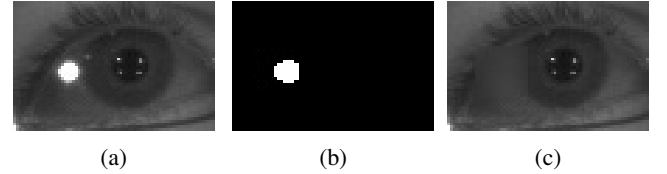


Fig. 16: A sample glare removal process: (a) input image, (b) obtained binary mask of the glare, (c) output image.

C. Glint Detection

Overview of the glint detection process is illustrated in Fig. S17. The process starts with histogram equalization on the input image following the glare removal process. It is then followed by a thresholding operation to obtain an initial binary mask indicating the candidate glints. This time, instead of a global thresholding, we use spatial adaptive thresholding in order to take into account spatial variations in illumination. Adaptive thresholding tunes thresholds for small regions of the image rather than a global threshold value for the whole image. Therefore, various thresholds are applied for different regions of the same image, resulting in more stable thresholding under varying illumination. We use OpenCV's adaptive thresholding function. The parameters *block size* and *C* (i.e., a constant subtracted from the mean) are set to 10% of the original image width and -100, respectively. The actual threshold value,

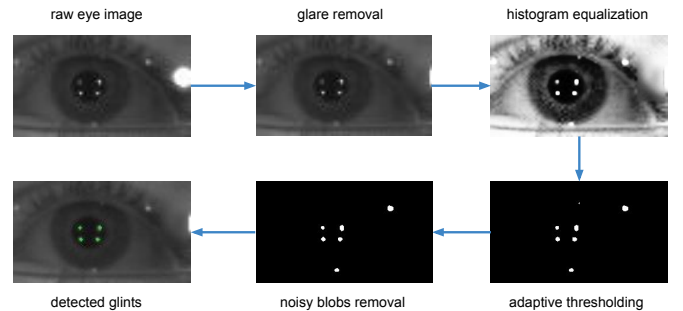


Fig. 17: Overview of the glint detection process.

$T(x,y)$, is a mean of the $block\ size \times block\ size$ neighborhood of (x, y) minus C . The adaptive thresholding is followed by morphological opening and closing operations to get rid of the small noisy blobs. We then perform connected component analysis to obtain the candidate glints, which are expected to form a trapezium shape since they emerge from the reflections of four LEDs located around the screen. If there are four or more candidate glints, we consider the shapes formed by any four-glints combination. The set of candidates whose convex hull has the highest match with a template shape representing the screen is considered as the final set of glints.

D. Pupil Detection

In comparison with glint detection process, pupil detection is a more troublesome process since the intensity of the pupil is more similar to its surrounding pixels. In this regard, two different approaches are performed throughout this paper, namely, bright-pupil based detection and dark-pupil based detection. Bright-pupil based approach leverages an optical phenomenon [36], which is similar to the red-eye effect in colored photography. This phenomenon is generated by placing an additional light source in the optical axis of the camera. It enables a high-contrast pupil region, and so, the pupil can more easily be detected. For this reason, it is widely preferred over the dark-pupil based detection in the literature. Thus, we as well utilized a bright-pupil based approach in the early phases of our development. However, we later switched to a dark-pupil based one due to the following limitations of the bright-pupil based method. Firstly, the bright-pupil response is related to the size of the pupil. In this respect, it is highly affected by the ambient illumination conditions. In addition, user's age and ethnicity play an important role in the pupil response, such that it works well for Caucasians and Hispanics, whereas the response is much poorer for Asians, as clearly shown in [47]. Besides, we observed that placing an additional light source per camera, especially in a multi-camera setting, significantly influences the eye glasses robustness due to the additional reflections caused by the increased number of light sources. In fact, using additional light sources may also harm the eyes of the user and increases the system's total power consumption. The following subsections describe the details of both approaches.

1) *Bright-pupil based approach*: This approach is originally suggested by [36] in order to robustly detect the pupil by leveraging the bright-pupil effect, which is generated when a light source is located in the optical axis of the camera. The main advantage of this approach is that the difference of dark and bright pupil images results in a high contrast pupil region. Inspired by Ebisawa's technique, we generated dark and bright-pupil effects by switching between off-axis and on-axis light sources in consecutive frames. When these images are obtained from a high frame rate camera, the difference image provides a high contrast pupil region as can be seen in Fig. S18. Once such a high contrast pupil region is obtained, we then proceed with the segmentation of the pupil and its center by performing a very similar image processing as in glint detection.

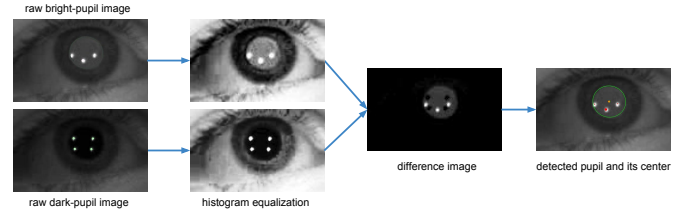


Fig. 18: Pupil detection using the bright-pupil approach.

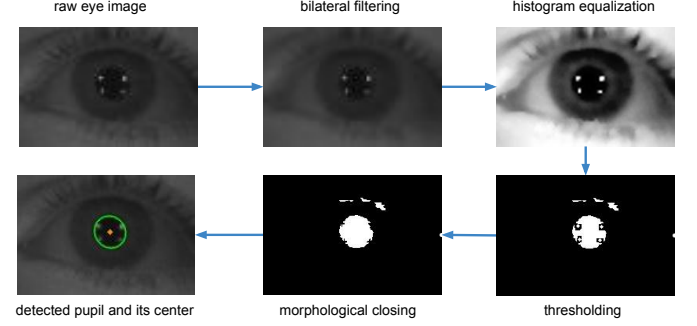
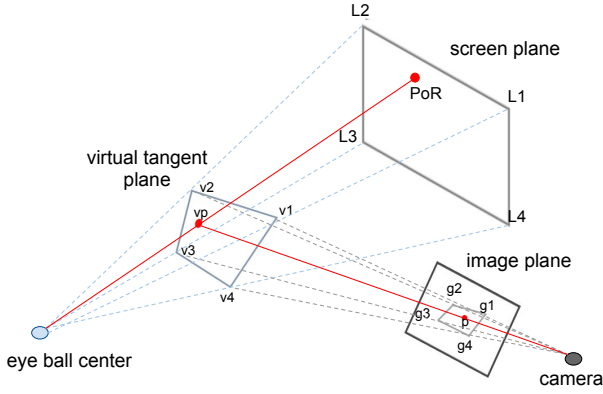


Fig. 19: Pupil detection using the dark-pupil approach.

2) *Dark-pupil based approach*: Dark-pupil based detection naturally requires a more sophisticated image processing in comparison to bright-pupil effect based approach since it does not exploit any special optical effect. Similar to glint detection process, we utilize well-known image processing algorithms on dark-pupil images. First of all, we perform bilateral filtering on the raw dark-pupil eye image to smooth the pupil region while still keeping the pupil-to-iris edges sharp. We then equalize the histogram to further enhance the contrast. Next, we approximate the average intensity within the pupil's dark regions. As some of the glints are within the pupil region, we discard the glints while calculating the average pupil intensity. We then remove the glints by filling them with the approximated average intensity. On the resulting image, we apply global thresholding by considering the average intensity within the pupil. We then invert the image to highlight the pupil blob. Nevertheless, few other blobs, which are at least as dark as the pupil region, such as eye lashes, eye lids, shades, etc., also remain in the binary image. In order to separate the actual pupil region from the noisy blobs, we iterate over all of them and apply morphological operators to determine the candidate pupil blobs. Among the candidates, we determine the final pupil by considering the shape, size, and the location of the blobs. Lastly, we determine the pupil center by calculating the center of gravity of the found pupil blob. The dark-pupil based detection process is shown with intermediate steps in Fig. S19.

E. Cross Ratio-based Gaze Estimation

We employ the original cross ratio method [48] for the estimation of the PoR. The cross ratio method is a projective geometry based gaze estimation technique for uncalibrated gaze estimation setups. It relies on the cross-ratio property, an

Fig. 20: Geometric setup in *cross ratio-based* gaze estimation.

invariant of projective space. Fig. S20 illustrates the geometric setup used by the cross ratio method.

In cross ratio method, a virtual tangent plane on the cornea surface, where the four glints (v_1, v_2, v_3, v_4) lie on, is assumed to exist. Hence, the polygon formed by the glints is the projection of the monitor. Another projection takes place from the corneal plane to the image plane, obtaining the glints (g_1, g_2, g_3, g_4) and the projection of the pupil center, p . As the virtual tangent plane on the cornea has the same planar projective transformation of the monitor and image planes, the pupil center on image plane corresponds to the PoR on the monitor.

The PoR on the monitor can be computed by the equality of the cross-ratios on the monitor plane, $CR_{monitor}$ and the camera image plane, CR_{image} (Fig. S21). The cross ratio is defined for four collinear points as:

$$CR(p_1, p_2, p_3, p_4) = \frac{|p_1 p_2| |p_3 p_4|}{|p_1 p_3| |p_2 p_4|}, \quad (7)$$

where

$$|p_i p_j| = \det \begin{bmatrix} p_i^x & p_j^x \\ p_i^y & p_j^y \end{bmatrix}. \quad (8)$$

The cross-ratio on the x axis of the monitor plane can be computed as follows:

$$CR_{monitor}^x(L_1, m_1, m_2, L_2) = \frac{(w - \frac{w}{2}) \hat{p}_x}{(w - \hat{p}_x) \frac{w}{2}} = \frac{\hat{p}_x}{w - \hat{p}_x}, \quad (9)$$

where w is the width of the monitor and \hat{p}_x is the x coordinate of the estimated gaze point p .

The corresponding cross-ratio of the image plane is:

$$CR_{image}^x(g_1, i_1, i_2, g_2) = \frac{|g_1 i_1| |i_2 g_2|}{|g_1 i_2| |i_1 g_2|}. \quad (10)$$

Since the cross-ratios of both configurations are equal, the estimated x coordinate of the PoR, \hat{p}_x , can be calculated as follows:

$$\hat{p}_x = \frac{w}{1 + CR_{image}^x}. \quad (11)$$

A similar derivation on the y axis gives the estimated y coordinate of the PoR, \hat{p}_y , as follows:

$$\hat{p}_y = \frac{h \cdot CR_{image}^y}{1 + CR_{image}^y}, \quad (12)$$

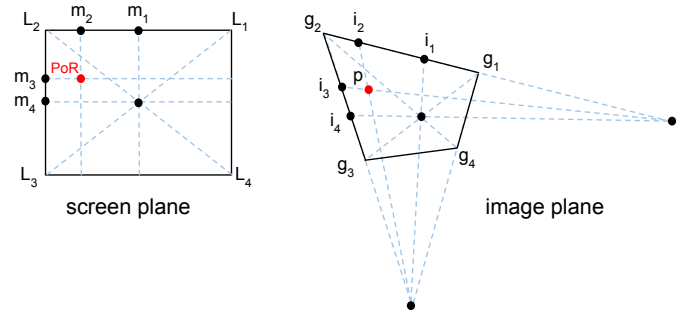


Fig. 21: Cross-ratio of image and screen points.

where h is the height of the monitor.

IX. FURTHER DETAILS ON OUR EVALUATIONS

This section describes the details of our evaluations on the user experiments that were not included in the main manuscript due to page limitations. Details of evaluation metrics are presented in Section IX-A, followed by further details on the collected dataset and experimental protocols in Section IX-B. In Section IX-C1, the results of user experiments on between-subject eye type robustness are explained. Lastly, real-time implementation details are provided in Section IX-D.

A. Evaluation Metrics

In our evaluations, the tracking performances are measured as the gaze estimation accuracy error, which is defined as the average displacement in degrees of visual angle ($^\circ$) between the target stimuli points and the estimated PoRs, using all raw samples. Neither temporal smoothing nor post-processing is applied in order to demonstrate the real impact of our framework and methods. For the real-time system, temporal smoothing can still be performed for a smoother tracking experience for the users.

$$Error_{pixel} = \frac{\sum_i^N \sum_j^K ||\mathbf{P}_i - \mathcal{F}(\mathbf{z}_{i,j}^*)||}{NK} \quad (13)$$

$$Error_{mm} = \frac{Error_{pixel}}{\text{pixel-to-mm ratio of monitor}} \quad (14)$$

$$Error_{\text{visual angle } (^\circ)} = \frac{Error_{mm}}{\text{user-to-monitor distance}} \frac{180}{\pi} \quad (15)$$

where \mathbf{P}_i and $\mathbf{z}_{i,j}^*$ denote the i^{th} target stimuli point and the estimated raw PoR of the j^{th} sample for the corresponding target point, respectively. User calibration model is denoted by \mathcal{F} . Total number of target points is denoted by N , and K samples (frames) are acquired per point during a test session. *pixel-to-mm ratio* is obtained from the monitor specifications¹. We note that the estimation errors are reported in degrees of visual angle ($^\circ$) since it is invariant to *user-to-monitor distance*. In addition, the estimation availability is defined as

¹In our evaluations, 1 pixel is equal to 0.27 mm on our 24-inch monitor. Consequently, 1° of visual angle error indicates ~ 39 pixels on the monitor when the user is at a distance of 60 cm.

Each participant was asked to follow 8 different experiments as described in Fig. S22 and Table II in the main manuscript. Experiment #2 being the default protocol, in the first three experiments, we analyze the system’s tolerance against varying illumination conditions by altering the ambient illumination (experiments #0 and #1). As our tracker’s main target scenario, the default illumination is considered as an office environment illuminated by indoor fluorescent lighting. Illumination robustness is then examined under two alternative conditions such as total darkness and sunlight. The setup was installed by the windows inside a regular office at EPFL, Switzerland. Total darkness was obtained by closing the window blinds and turning off the indoor lights. On the other hand, the experiments with sunlight were conducted on sunny days and users were exposed to sunlight through the windows. The remaining five experiments were conducted to evaluate the system’s robustness against head movements as described in the main manuscript. As our evaluation targeted natural human-computer interaction scenarios, we tried to collect the ground truth data as natural as possible for the subjects. For instance, we did not use a chin rest to keep the subject’s head still and to keep the eye within the cameras’ FoV to capture

1) *Eye Type Robustness:* In addition to the robustness analyses on head movements, use of eyewear, variations in illumination, which are provided in the main manuscript, we here present the details of our analysis on the proposed framework’s tolerance against between-subject eye type variations. Since certain eye type related factors, e.g., eye color, eye shape, pupil response, may affect the performance of the eye trackers [47], we evaluated our system’s performance under varying eye types across the subjects. Fig. S23 shows sample eye type and color variations from the dataset. Firstly, since the iris color has a great influence on both the pupil size and opening of eyelids when exposed to various illumination conditions, we categorized the subjects into two groups according to the

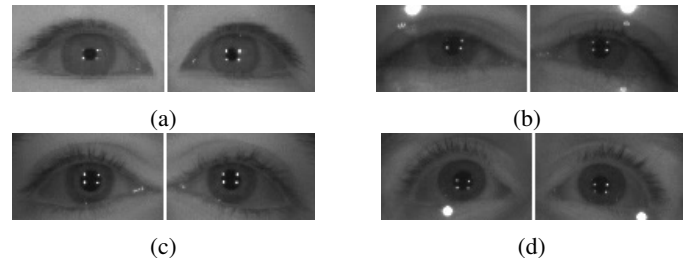


Fig. 23: Sample eye appearances from the dataset. (a) Asian dark eyes without glasses, (b) Asian dark eyes with glasses, (c) Caucasian dark eyes without glasses, (d) Caucasian dark eyes with glasses.

eye color such as dark-eyed ones (10 subjects) and light-eyed (10 subjects). On average over all experiments, dark- and light-eyed groups achieve 1.15° with 96.2% availability and 1.44° with 93.3% performances, respectively. However, the results may be biased towards the dark-eyed group since most of the subjects who do not wear eye glasses are within this group. An interesting result is that the performance difference between the light-eyed (1.33°) and dark-eyed groups (0.92°) is especially large under sunlight (experiment #0). The reason is that the pupil size and eye opening are affected more for the light-eyed subjects in comparison with the dark-eyed subjects due to their higher sensitivity to the sunlight. Table SVII shows average estimation accuracy errors and estimation availabilities in detail for each experiment in several categories.

It is also important to note that the pupil detection method has an influence on the robustness to eye color variations. As discussed in Section VIII-D, bright-pupil based method is frequently employed by the previous work as the feature detection is simpler compared to dark-pupil based one. However, in our preliminary experiments, we observed that dark-pupil based feature detection is less sensitive to the variations in eye color. In bright-pupil based method, the accuracy of the pupil detection heavily relies on the pupil response (brightness), which is highly affected by users' momentary pupil size that varies according to the eye color, ethnicity, and ambient illumination. Therefore, in our final framework, we employ dark-pupil based feature detection in order to become less sensitive to eye type and illumination factors. We plan to give a structured and quantitative comparison in our future work.

Furthermore, we categorized the subjects by their eye shape into two groups: Asian eyes (2 subjects) and non-Asian eyes (18 subjects) to analyze the impact of the eye shape. Our results show that Asian eyes (1.58° with 93.35% availability) perform worse than non-Asian eyes (1.25° with 97.7% availability). Yet, the system can still accurately estimate the gaze for our Asian subjects. The decrease in the availability may indicate that the feature detection for them might be more challenging due to the eye shape. Nevertheless, it is difficult to make a strong conclusion as the two sets are highly imbalanced. In addition, we note that there is a significant variation across Asian eyes [49], [50]. The eyes may be of any shape including round, narrow, almond, hooded, triangular, prominent, or deep-set. In addition, the eyes can be a single eyelid, low/incomplete eyelid crease, and double eyelid. For some of these eye shapes (e.g., narrow, hooded), eye tracking could be highly challenging as the creation and detection of the gaze features could be exigent. Our dataset currently do not contain such challenging eye types. In our future work, we plan to recruit a higher number of Asian subjects and increase the variation in eye type to obtain a more reliable analysis.

D. Real-time Implementation

One of the high-priority objectives of this work is to achieve real-time eye tracking performance, so that the eye tracker can be utilized in practice. In this regard, we developed a complete multi-camera gaze estimation library in C++. In order to implement image processing and computer vision algorithms,

we mostly utilized Open Computer Vision (OpenCV) library². Localization of facial landmarks were performed using a supervised descent method (SDM)-based face tracker³. Furthermore, to achieve real-time tracking performance, Open Multi-Processing (OpenMP⁴) application programming interface was utilized for the parallelization of our library implementation.

The computational complexity of the system is lower than 3D model-based methods as the gaze estimation relies on perspective geometry transformations and computation of cross ratios. This enables to achieve a real-time implementation without requiring any particular performance optimization. In our implementation, the most computationally expensive process is face detection/tracking. Gaze estimation for both eyes using cross ratio algorithm, user calibration, and adaptive fusion processes require much lower computational effort. For instance, these three processes take only ~ 8 ms on a PC with Intel i7 3.2 GHz processor, whereas face tracking itself takes ~ 24 ms. Our current three-camera prototype system can simultaneously output PoRs for both eyes as well as an overall PoR at ~ 30 frames-per-second (fps) with a mean estimation accuracy error of $\sim 1^\circ$ of visual angle. We also note that there is still much room for computationally improving our implementation to reach higher frame rates. For instance, the computationally expensive face tracking process can be replaced with a simpler or faster face or eye region tracker, such as local binary features (LBF)-based face tracking [51], or one millisecond face alignment with an ensemble of regression trees [52]. As the feature extraction process does not require precisely located facial landmarks from a face tracker, but rather needs a rough estimate of the eye region, simpler trackers can be employed to reach higher frame rates while achieving similar estimation accuracies. In addition, the implementation of remaining processes can further be optimized. We leave such computational improvements as future work.

²<http://opencv.org/>

³www.humansensing.cs.cmu.edu/intraface/download_functions_cpp.html

⁴<http://www.openmp.org/>

TABLE VI: Head pose statistics (in $^{\circ}$) of two subjects from the dataset. The head pose angles are estimated with respect to the bottom camera view separately on calibration and six individual test sessions relevant to head movements.

	Session	Exp No	Yaw				Pitch				Roll			
			Min	Max	Std	Mean	Min	Max	Std	Mean	Min	Max	Std	Mean
Subject #8	Calib.	#2	-13.3	2.6	4.7	-4.8	-13.6	4.9	5.3	-3.6	-6.2	0.1	1.7	-3.2
	Test	#2	-11.3	6.2	4.6	-2.6	-16.5	3.8	5.1	-5.3	-6.7	0.1	1.5	-2.7
		#3	-20.9	31.2	11.3	-1.5	-21.3	6.7	5.6	-3.4	-20.1	13.5	5.7	-3.9
		#4	-21.9	10.5	9.1	-3.4	-15.9	7.2	5.6	-1.8	-12.8	0.7	3.4	-5.3
		#5	-15.8	10.2	6.2	-3.6	-5.7	5.6	2.9	-0.2	-9.4	0.2	2.1	-4.6
		#6	-12.9	13.2	6.3	-2.4	-16.9	8.4	4.9	-2.3	-11.9	-2.6	2.2	-8.5
		#7	-15.2	9.9	5.3	-3.5	-8.2	6.4	2.9	-0.4	-3.7	4.5	1.8	0.5
	Subject #18	Calib.	#2	-14.1	22.9	13.5	2.6	-21.1	0.9	6.9	-9.6	-4.4	4.4	2.4
Test		#2	-15.8	22.9	12.3	3.7	-23.1	-0.7	7.1	-10.2	-4.2	2.4	1.6	-1.1
		#3	-24.5	19.4	10.4	-0.9	-20.8	7.9	6.2	-7.4	-25.5	16.7	8.7	-2.7
		#4	-18.1	22.9	12.7	0.2	-24.3	-1.9	6.2	-12.6	-6.3	1.9	2.2	-1.6
		#5	-15.7	19.1	10.5	0.6	-21.3	-2.3	4.7	-10.2	-5.4	1.9	1.4	-2
		#6	-18.1	18.9	10.2	1.9	-22.9	3.6	7	-8.4	-14.2	-6.5	1.6	-9.4
		#7	-17.2	28.2	11.9	3.6	-22.6	4.9	6.8	-7.8	1.1	7.4	1.6	4.4

TABLE VII: Mean estimation accuracy errors and gaze availabilities achieved by various single and multi-view setup configurations on each of the user experiments.

Configurations			Exp 0		Exp 1		Exp 2		Exp 3		Exp 4		Exp 5		Exp 6		Exp 7	
camera	eye		($^{\circ}$)	(%)	($^{\circ}$)	(%)	($^{\circ}$)	(%)	($^{\circ}$)	(%)	($^{\circ}$)	(%)	($^{\circ}$)	(%)	($^{\circ}$)	(%)	($^{\circ}$)	(%)
single-camera	right	left	1.71	50.6	1.68	51.6	1.59	57.3	2.04	46.8	1.87	36.3	2.06	49.6	1.84	51.1	1.53	37.5
	right	right	1.5	60.4	1.86	68.1	1.52	69.6	2.16	58.6	2.27	41.7	2.26	63.2	1.83	66.7	1.55	65.1
	right	both	1.55	74.4	1.6	74.9	1.41	77.6	2	69.7	2.11	52	2.07	75.2	1.77	73.7	1.35	69.4
	left	left	1.64	62.1	2.02	68.9	1.54	65.8	2.07	57	2.1	47.4	2.18	53.1	1.88	47.6	1.68	70.4
	left	right	1.55	51.4	1.86	56.1	1.49	56.9	1.86	44.2	1.83	44.7	2.28	51.2	2.08	33.8	1.75	62.1
	left	both	1.5	73.1	1.8	78.3	1.36	79.4	1.88	68.3	1.79	61.8	2.07	71.9	1.77	58.7	1.51	83.2
	bottom	left	1.68	77	1.86	78.1	1.50	81.8	1.93	72.1	1.96	64.7	1.99	67.7	1.79	77.6	1.63	73.4
	bottom	right	1.65	74.6	1.86	79.5	1.54	79.2	1.90	68.3	2.05	64.8	2.32	67.4	1.76	75.5	1.58	75.1
	bottom	both	1.46	91.2	1.51	94.6	1.30	93.6	1.67	87	1.73	82.4	1.81	83.9	1.33	92.5	1.32	90.8
	overall		1.07	96.2	1.22	98.4	0.99	97.2	1.45	92.2	1.52	92.4	1.60	93.7	1.10	95.2	1.12	95.5
multi-view	w/ perfect vis.		0.86	98	1.02	98.5	0.77	98.8	1.20	94.8	1.21	94.9	1.18	98.8	0.79	98.8	0.81	98.9
	w/ contacts		0.83	96.8	1.05	99.7	0.76	98.9	1.23	92.5	1.41	97.5	1.17	99.1	0.88	99	1.02	98.5
	w/o glasses		0.98	97	1.11	99.1	0.89	98.6	1.38	94.2	1.40	96.5	1.44	96.8	0.92	98.9	1.01	98.3
	w/ glasses		1.39	93.4	1.63	95.6	1.38	91.9	1.68	84.4	1.95	76.8	2.19	82	1.77	81.4	1.51	85
	dark-eyed		0.92	96.7	1.16	97.8	0.86	98.2	1.29	93.8	1.42	93.5	1.46	96.4	1.05	95.9	1.03	97
	light-eyed		1.33	95.4	1.33	99.3	1.22	95.7	1.70	89.5	1.68	90.5	1.85	89.1	1.18	94	1.26	93



(a) Illumination variations, i.e., experiments #2, #0, #1.



(b) Depth movements, i.e., experiments #2, #5, #4.



(c) Horizontal movements, i.e., experiments #2, #6, #7.

Fig. 24: Sample images from the collected dataset: (left column) right camera view, (middle column) bottom camera view, and (right column) left camera view.